

# 1 Less atmospheric radiative heating by dust due to the synergy of 2 coarser size and aspherical shape

3 Akinori Ito<sup>1</sup>, Adeyemi A. Adebisi<sup>2,3</sup>, Yue Huang<sup>2</sup>, and Jasper F. Kok<sup>2</sup>

4 <sup>1</sup>Yokohama Institute for Earth Sciences, JAMSTEC, Yokohama, Kanagawa, 236-0001, Japan.

5 <sup>2</sup>Department of Atmospheric and Oceanic Sciences, University of California, Los Angeles, CA 90095, USA.

6 <sup>3</sup>Department of Life and Environmental Sciences, University of California - Merced

7 *Correspondence to:* Akinori Ito (akinorii@jamstec.go.jp)

8 **Abstract.** Mineral dust aerosols cool and warm the atmosphere by scattering and absorbing solar (short-wave: SW)  
9 and thermal (long-wave: LW) radiation. However, significant uncertainties remain in dust radiative effects, largely  
10 due to differences in the dust size distribution and spectral optical properties simulated in Earth system models. Dust  
11 models typically underestimate the coarse dust load (more than 2.5  $\mu\text{m}$  in a diameter) and assume a spherical shape,  
12 which leads to an overestimate of the fine dust load (less than 2.5  $\mu\text{m}$ ) after the dust emissions in the models are scaled  
13 to match observed dust aerosol optical depth at 550 nm (DAOD<sub>550</sub>). Here, we improve the simulated dust properties  
14 with datasets that leverage measurements of size-resolved dust concentration, asphericity factor, and refractive index  
15 in a coupled global chemical transport model with a radiative transfer module. After the adjustment of size-resolved  
16 dust concentration and spectral optical properties, the global and annual average of DAOD<sub>550</sub> from the simulation  
17 increases from 0.023 to 0.029 and falls within the range of a semi-observationally-based estimate ( $0.030 \pm 0.005$ ).  
18 The reduction of fine dust load after the adjustment leads to a reduction of the SW cooling at the Top Of the  
19 Atmosphere (TOA). To improve agreement against a semi-observationally-based estimate of the radiative effect  
20 efficiency at TOA, we find that a less absorptive SW dust refractive index is required for coarser aspherical dust. Thus,  
21 only a minor difference is estimated for the net global dust radiative effect at TOA ( $-0.08$  vs.  $-0.00 \text{ W}\cdot\text{m}^{-2}$  on a global  
22 scale). Conversely, our sensitivity simulations reveal that the surface warming is substantially enhanced near the  
23 strong dust source regions (less cooling to  $-0.23$  from  $-0.60 \text{ W}\cdot\text{m}^{-2}$  on a global scale). Thus, less atmospheric radiative  
24 heating is estimated near the major source regions (less heating to 0.15 from 0.59  $\text{W}\cdot\text{m}^{-2}$  on a global scale), because  
25 of enhanced LW warming at the surface by the synergy of coarser size and aspherical shape.

## 26 1 Introduction

27 Mineral dust aerosols can both cool and warm the climate, but how much dust aerosols net influence global  
28 climate is highly uncertain (Penner, 2019). Global dust modeling studies have suggested that mineral dust exerts  
29 global and annual mean aerosol radiative effect (RE) between  $-0.6$  and  $+0.2 \text{ W m}^{-2}$  at the Top Of the Atmosphere  
30 (TOA) and between  $-0.2$  and  $-2.7 \text{ W m}^{-2}$  at the surface (Miller and Tegen, 1998; Balkanski et al., 2007; Tanaka et  
31 al., 2007; Takemura et al., 2009; Räisänen et al., 2013; Zhao et al., 2013; Albani et al., 2014; Colarco et al., 2014;  
32 Heald et al., 2014; Di Biagio et al., 2020; Tuccella et al., 2020). Whereas a negative RE corresponds to the cooling of  
33 the global system when the sunlight is reflected to space, a positive RE corresponds to an overall warming of the  
34 Earth-atmosphere system by trapping incident short-wave (SW) and outgoing long-wave (LW) radiation. Radiative  
35 effect by dust aerosols perturbs surface temperature, wind speed, rainfall, and vegetation cover, which may induce

36 feedback on dust emissions (Perlwitz et al. 2001; Miller et al., 2004a; Colarco et al., 2014). The climate feedback does  
37 not only depend on RE at TOA or the surface alone but also on the difference to the value at TOA and surface, which  
38 represents radiative heating within the atmosphere (Miller et al., 2004b; Yoshioka et al., 2007; Lau et al., 2009). The  
39 large uncertainties in quantifying the dust RE in the models are mainly propagated from the large spatial heterogeneity  
40 and temporal variability of mineral dust abundance and the physicochemical properties (e.g., size distribution, mineral  
41 composition, and shape), as well as the ground surface characteristics and atmospheric properties (e.g., surface  
42 reflectance, temperature, and atmospheric absorption) (Sicard et al., 2014; Lacagnina et al., 2015; Li and Sokolik,  
43 2018). The model errors in dust size distribution and particle shape can lead to an overestimate of fine dust load after  
44 the dust emissions in the models are scaled to match observed dust aerosol optical depth at 550 nm (DAOD<sub>550</sub>). The  
45 corresponding overestimate of SW cooling might be compensated for in models by using a refractive index that is too  
46 absorbing (Di Biagio et al., 2019, 2020), which depends on the mineral composition of the dust. We regard “fine” and  
47 “coarse” dust as dust particles with a diameter less than 2.5  $\mu\text{m}$  (i.e., PM<sub>2.5</sub>) and between 2.5 and 20  $\mu\text{m}$ , respectively.  
48 Below, we provide a brief discussion of the effects of the dust size distribution, particle shape, and mineral  
49 composition on dust radiative effects.

50 First, there has been increased attention paid to the importance of accurately predicting the abundance of coarse  
51 dust for the global energy balance (Kok et al., 2017; Song et al., 2018; Di Biagio et al., 2020; Adebisi and Kok, 2020).  
52 The coarser particles are expected to be more prevalent closer to the source regions, as they fall much faster than finer  
53 particles (Mahowald et al., 2014). For instance, the lifetime of dust aerosols larger than 30  $\mu\text{m}$  in diameter is less than  
54 12 h in most cases except in large haboobs (Ryder et al., 2013). Current models, however, cannot accurately simulate  
55 observed transport of coarse dust particles across the Atlantic (Weinzierl et al., 2017; Ansmann et al., 2017), although  
56 several hypotheses have been proposed to explain measurements of giant dust particles (larger than 63  $\mu\text{m}$  in diameter)  
57 relatively far from source regions (van der Does et al., 2018). The potential mechanism for long-range transport of  
58 giant dust particles is that the uplift events of coarse dust can be induced by a nocturnal low-level jet or cold pool  
59 outflow from mesoscale convective systems (i.e., haboobs) (Rosenberg et al., 2014; Ryder et al., 2019). At higher  
60 elevation, electrostatic forces might retard the settling of coarse and giant dust particles and thus may facilitate the  
61 transport of these particles over longer distances (Harrison et al., 2018; Toth et al., 2019). Other missing processes  
62 that affect the transport and deposition of giant particles would also need to be incorporated into the models to  
63 reproduce the measurements of the size distribution over the open ocean (van der Does et al., 2018). The coarse dust  
64 particles scatter and absorb both the solar and thermal radiation, causing a net warming effect at TOA. In contrast, the  
65 fine dust particles principally scatter SW radiation, causing a net cooling effect. Since coarse dust tends to warm the

66 climate, the underestimation of the abundance of coarse dust causes Earth system models to underestimate the  
67 warming near the dust source regions.

68 Second, previous studies have shown that the SW radiative effect of dust asphericity on climate simulations is  
69 minor on a global scale, partly because the larger DAOD is compensated for by the larger asymmetry parameter of  
70 aspherical dust, which reduces the amount of radiation scattered backward to space (Räsänen et al., 2013; Colarco et  
71 al., 2014). Moreover, non-spherical calcium-rich dust particles can be converted to spherical particles, due to  
72 heterogeneous reactions with nitrate and sulfate on these particles, especially over polluted regions (Laskin et al.,  
73 2005; Matsuki et al., 2005). As the plumes move downwind to the oceans, the dust aerosols can be aggregated with  
74 sea salt in the marine boundary layer, which leads to more spherical shapes and larger sizes (Zhang and Iwasaka,  
75 2004). However, the assumption of spherical shape in models leads to a substantial underestimation of the extinction  
76 efficiency and thus DAOD near the strong source regions, mainly because the assumption of sphericity causes an  
77 underestimation of the surface-to-volume ratio compared to aspherical dust (Kok et al., 2017, 2021; Hoshyaripour et  
78 al., 2019; Tuccella et al., 2020). Radiative effect efficiency is often used for the evaluation of the models and is defined  
79 as the gradient of a linear least squares fit applied to AOD and dust radiative effect at each two-dimensional (2-D)  
80 grid box ( $W \cdot m^{-2} AOD^{-1}$ ). Thus, the estimates of the dust radiative effect efficiency could be biased, in part, due to  
81 large uncertainties associated with the spherical assumption on AOD retrieval (Zhou et al., 2020).

82 Third, the dust refractive index is often derived from measurements based on dust or individual mineral particles  
83 (Bedidi and Cervelle, 1993; Long et al., 1993; Di Biagio et al., 2017, 2019; Stegmann & Yang, 2017). Indeed, most  
84 dust particles are internal mixtures of various mineral compositions and irregular shapes (Reid, 2003; Wiegner et al.,  
85 2009; Wagner et al., 2012). In desert soils, iron (Fe) oxides are generally hematite ( $\alpha\text{-Fe}_2\text{O}_3$ ) and goethite (FeOOH),  
86 which cause soil-derived dust absorption at ultraviolet (UV) and visible wavelengths (Sokolik and Toon, 1999;  
87 Balkanski et al., 2007). These two minerals have distinct optical properties, which might cause various intensities of  
88 SW absorption and thus RE of dust aerosols (Lafon et al., 2016). The dust complex refractive index in the LW also  
89 depends on the particle mineralogical composition (Sokolik et al., 1998). Di Biagio et al. (2017) found a linear  
90 relationship between the magnitude of the imaginary refractive index at 7.0, 9.2, and 11.4  $\mu\text{m}$  and the mass  
91 concentration of calcite and quartz absorbing at these wavelengths. However, the speciation of dust into its mineral  
92 components inherently comprises uncertainties on soil mineralogy, mineral content in size-segregated dust particles,  
93 and refractive index of mineral, partly due to the differences in prescribed parameters such as the particle size. The  
94 atmospheric aging of Fe-containing aerosols can further modulate the optical properties of Fe oxides (Ito et al., 2018)  
95 and organic carbon (Al-Abadleh, 2021), while the photochemical transformation of Fe oxides from lithogenic sources  
96 due to atmospheric processing is relatively limited ( $< 10\%$ ), compared to pyrogenic sources (Ito et al., 2019).

97 Here, we focus on the influence of the size-resolved abundance of aspherical dust on the aerosol radiative effects  
98 in a coupled global chemical transport model (IMPACT) (Ito et al., 2020 and references therein) with a radiative  
99 transfer module (RRTMG) (Iacono et al., 2008). We improve the accuracy of these simulations by correcting the bias  
100 in size-resolved dust concentration with the Dust Constraints from joint Observational-Modelling-Experimental  
101 analysis (DustCOMM) data set (Adebiyi et al., 2020), as well as by considering the aspherical shape (Huang et al.,  
102 2020, 2021). We then explore the sensitivity to dust refractive index.

## 103 **2 Methods**

104 We examined the dust radiative effects using ten combinations of different numerical experiments that varied  
105 (1) the simulated dust concentration and their size distribution, (2) particle shape, and (3) mineralogical composition  
106 (Tables 1 and 2). Two RRTMG calculations used the hourly averaged aerosol concentrations calculated from one  
107 IMPACT model simulation (E1 and E3) (denoted as “IMPACT”). The two sensitivity experiments were handled in  
108 the RRTMG calculations performed with the distinction between spherical and non-spherical dust and different  
109 refractive indices. We denoted “Sphere” when the RRTMG calculations used the spherical assumption on the particle  
110 shape, while the IMPACT model considered asphericity in calculation of gravitational settling velocities. On the other  
111 hand, we denoted “Asphere” when the dust asphericity was also considered in the RRTMG calculations. Subsequently,  
112 the simulated dust concentration and the size distribution were adjusted to the semi-observationally-based  
113 concentrations (Adebiyi and Kok, 2020) in another chemical transport model simulation, which was performed with  
114 the five RRTMG calculations (E4, E5, E6, E8, and E9) (denoted as “DustCOMM”). The term “semi-observationally-  
115 based” is used for DustCOMM, DAOD<sub>550</sub>, and dust radiative effect efficiency when the estimates are based on the  
116 combination of observations and models. We examined different refractive indices for the dust mineralogy to represent  
117 the regional variations in refractive indices (denoted as “Mineral”, “DB17”, “DB19”, “V83”, “Less SW”, “More LW”,  
118 “More SW”, and “Less LW”). Thus, the other three experiments (E2, E7, and E10) were calculated from the model  
119 output with a post-processor. DustCOMM-Asphere-DB19-V83 (E2) was obtained from combination of DustCOMM-  
120 Asphere-DB19-DB17 (E4) for SW and DustCOMM-Asphere-Mineral-V83 (E6) for LW. DustCOMM-Asphere-Less-  
121 More (E7) was obtained from combination of DustCOMM-Asphere-Less-Less (E8) for SW and DustCOMM-  
122 Asphere-More-More (E9) for LW. DustCOMM-Asphere-More-Less (E10) was obtained from combination of  
123 DustCOMM-Asphere-More-More (E9) for SW and DustCOMM-Asphere-Less-Less (E8) for LW. These sensitivity  
124 simulations and their radiative effects are summarized in Tables 1 and 2, respectively, with more details below. In  
125 section 2.3, we describe the DustCOMM data set used to adjust (1) size-resolved abundance of dust concentration. In  
126 section 2.4, we describe the adjustment factor of (2) particle shape for spectral optical properties. In section 2.5, we

127 describe differences in spectral refractive indices due to (3) different mineralogical compositions for the radiative flux  
128 calculation.

## 129 **2.1 Aerosol chemistry transport model**

130 This study used the Integrated Massively Parallel Atmospheric Chemical Transport (IMPACT) model (Ito et  
131 al., 2020 and references therein). Simulations were performed for the year 2016, using a horizontal resolution of  
132  $2.0^{\circ} \times 2.5^{\circ}$  for latitude by longitude and 47 vertical layers. The chemical transport model was driven by the Modern  
133 Era Retrospective analysis for Research and Applications 2 (MERRA-2) reanalysis meteorological data from the  
134 National Aeronautics and Space Administration (NASA) Global Modeling and Assimilation Office (GMAO) (Gelaro  
135 et al., 2017). Thus, the radiative feedback of the dust aerosol on the climate was not considered in this study.

136 The model simulated the emissions, chemistry, transport, radiation, and deposition of major aerosol species,  
137 including mineral dust, black carbon (BC), particulate organic matter (POM), sulfate, nitrate, ammonium, and sea  
138 spray aerosols, and their precursor gases. Dust emissions were dynamically simulated using a physically-based  
139 emission scheme (Kok et al., 2014; Ito and Kok, 2017) with the soil mineralogical map (Journet et al., 2014; Ito and  
140 Shi, 2016). Atmospheric processing of mineral dust aerosols, during transport, were projected for four distinct aerosol  
141 size bins ( $<1.26 \mu\text{m}$ ,  $1.26\text{--}2.5 \mu\text{m}$ ,  $2.5\text{--}5 \mu\text{m}$ , and  $5\text{--}20 \mu\text{m}$  of diameter). In this version of the IMPACT model, two  
142 modes were used for sulfate aerosol (nuclei and accumulation mode), and two moments were predicted within each  
143 mode (sulfate aerosol number and mass concentration) (Liu et al., 2005). The surface coating of sulfate on dust  
144 aerosols occurred because of the condensation of sulfuric acid gas on their surfaces, coagulation with sulfate aerosol,  
145 and formation in aqueous reactions within cloudy regions of the atmosphere (Liu et al., 2005). The heterogeneous  
146 uptake of nitrate, ammonium, and water vapor by each aerosol for each size bin was interactively simulated in the  
147 model following a hybrid dynamical approach (Feng and Penner, 2007). Five types of aerosols (i.e., dust, nucleated  
148 sulfate, carbonaceous aerosols from fossil fuel combustion, carbonaceous aerosols from biomass burning, and sea salt)  
149 were assumed to be externally mixed in each size bin for the computation of spectral optical properties (Xu and Penner,  
150 2012). To derive atmospheric concentration of mineral composition for dust aerosol, “tagged” tracer was used for  
151 each size-resolved mineral source. The direct emissions of dust were evenly distributed in mixing ratio throughout the  
152 planetary boundary layer. The global scaling factor of dust emission was determined from the comparison of the model  
153 results with ground-based AOD measurements near the dust source regions prior to the adjustment to the DustCOMM  
154 (Kok et al., 2014; Ito and Kok, 2017). In recent review papers, multi-model evaluations of aerosol iron concentrations  
155 and their solubilities have been comprehensively summarized on global and regional scales (Myriokefalitakis et al.,  
156 2018; Ito et al., 2021).

157 To improve the accuracy of our simulations of mineral dust, we made several upgrades to the on-line emission  
158 and gravitational settling schemes used in Ito et al. (2020). The dust emissions were extremely sensitive to soil  
159 moisture, and thus the bias was adjusted with satellite observations (Ito and Kok, 2017). However, the satellite  
160 measurements were only available every other day, depending on location. The Soil Moisture Active Passive (SMAP)  
161 Level-4 Soil Moisture data product addressed these limitations by merging the satellite observations into a numerical  
162 model of the land surface water and energy balance while considering the uncertainty of the observations and model  
163 estimates (Reichle et al., 2019). In this work, we utilized the 3-hourly data of soil moisture derived from the SMAP  
164 for barren and open shrublands separately (Reichle et al., 2018). To achieve this, we used the MODerate resolution  
165 Imaging Spectroradiometer (MODIS) land cover map at 500 m resolution to calculate the fraction of barren and open  
166 shrublands in each ground surface layer (Friedl et al., 2019)

167 Compared to the assumption on spherical shapes of aerosols, the dust asphericity increased aerodynamic drag  
168 at a given volume and mass, and thus increased gravitational settling lifetime by about 20% (Huang et al., 2020). Here,  
169 we implemented a globally averaged asphericity factor of 0.87 (Huang et al., 2020) to the gravitational settling scheme  
170 for mineral dust. Nevertheless, the lifetime of the dust aerosol for the largest-size bin in the IMPACT model, even  
171 after accounting for asphericity (1.4 days for 5–20  $\mu\text{m}$  of diameter), was significantly shorter than an ensemble of  
172 model results ( $2.1 \pm 0.3$  days for the mass mean diameter of 8.3  $\mu\text{m}$ ) (Kok et al., 2017). The impact of this  
173 underestimate of atmospheric lifetime is explored using the DustCOMM data set, as was summarized in Table 2 (E3  
174 – E4).

## 175 **2.2 Integration of IMPACT and RRTMG**

176 To improve the accuracy of our simulations of dust RE, we made upgrades to the radiative transfer calculations  
177 (Ito et al., 2018 and references therein). In this study, we integrated the Rapid Radiative Transfer Model for GCMs  
178 (RRTMG) online within the IMPACT model to calculate the radiative fluxes associated with atmospheric aerosols.  
179 RRTMG is a radiative transfer code that calculates the SW and LW atmospheric fluxes (Iacono et al., 2008). Given  
180 the size range of dust particles, scattering and absorption in the on-line model were described in terms of Mie theory.  
181 Assuming homogeneous spherical particles, the spectral optical properties such as the mass extinction coefficient,  
182 single scattering albedo, and asymmetry parameter were calculated using a look-up table as a function of refractive  
183 index and size parameter (Xu and Penner, 2012). The impact of this spherical assumption is explored using aspherical  
184 factor, as was summarized in Table 2 (E5 – E4).

185 The mineral dust particles were assumed to follow prescribed size distributions within each size bin (Liu et al.,  
186 2005). In applying the look-up table, the size spectrum for mineral dust was divided into 30 sub bins (Wang and

187 Penner, 2009). As for the SW, the particle size increased with the uptake of sulfate, nitrate, ammonium, and water by  
188 the aerosols (Xu and Penner, 2012). These coating materials on aerosol cores were treated as internally mixed with  
189 each aerosol core in each size bin. Thus, the coating materials on dust only can reduce solar absorption of mineral  
190 dust. Subsequently, these optical properties were used by the RRTMG to calculate RE based on dust mixing ratio  
191 distributions in the IMPACT model. The dust RE was estimated as the difference in the calculated radiative fluxes  
192 with all aerosols and with all aerosols except the dust aerosols coated with sulfate, nitrate, ammonium, and water for  
193 each bin. As the LW scattering was not accounted for in the RRTMG, we multiplied the LW radiative fluxes by the  
194 adjustment factors of  $1.18 \pm 0.01$  and  $2.04 \pm 0.18$  for the dry particles at the surface and TOA (Dufresne et al., 2002),  
195 following Di Biagio et al. (2020). The larger adjustment factor at TOA reflects the fact that the upward LW radiation  
196 emitted from the ground surface can be trapped through scattering and absorption compared to the surface.

197 The broadband direct and diffuse albedos for both the UV visible and visible IR were specified from the hourly  
198 MERRA-2. The surface emissivity was based on the hourly MERRA-2. Long-lived greenhouse gas concentrations  
199 were obtained from historical greenhouse gas concentrations for climate models (Meinshausen et al., 2017). Water  
200 vapor concentrations were specified according to the MERRA-2. Cloud optical properties were calculated based on  
201 the liquid and ice visible optical depths from the MERRA-2, prescribing effective radii of 10  $\mu\text{m}$  for water droplets  
202 and 25  $\mu\text{m}$  for ice particles, respectively (Gettelman et al., 2010; Heald et al., 2014).

### 203 **2.3 DustCOMM dataset and sensitivity experiments to size-resolved dust concentration**

204 Dust Constraints from joint Observational-Modelling-experiMental analysis (DustCOMM) is a dataset of  
205 three-dimensional (3-D) dust properties obtained by combining observational, experimental, and modeling constraints  
206 on dust properties. While details can be found in Adebisi et al. (2020) and Adebisi and Kok (2020), we provide a  
207 brief overview here. First, DustCOMM's constraint on the 3-D dust size distribution combines dozens of previously  
208 published in-situ measurements of dust size distributions taken during several field campaigns, with an ensemble of  
209 climate model simulations. The framework used those in-situ measurements first to constrain the globally averaged  
210 size distribution (Adebisi and Kok, 2020), which is used subsequently to adjust the bias in an ensemble of six global  
211 model simulations (Adebisi et al., 2020). The constraints on dust size distribution range from 0.2  $\mu\text{m}$  to 20  $\mu\text{m}$  in  
212 diameter, where a generalized analytical function describes the sub-bin distribution based on brittle fragmentation  
213 theory (Kok, 2011). The second DustCOMM product – atmospheric dust mass loading – combines the constraints on  
214 dust size distribution with constraints on dust extinction efficiency and dust aerosol optical depth (Adebisi et al., 2020).  
215 The constraints on dust extinction efficiency used the single-scattering database of Meng et al. (2010) and leveraged  
216 measurements of the dust index of refraction as well as accounts for the non-spherical shape of dust particles (Kok et

217 al., 2017). For this, we approximate dust as tri-axial ellipsoidal particles described by the globally representative  
 218 values of measured dust aspect ratio (the length-to-width ratio), and the height-to-width ratio (HWR) obtained from  
 219 Huang et al. (2020). Furthermore, the dust aerosol optical depth used to obtain the dust mass loading combines the  
 220 semi-observationally-based dataset from Ridley et al. (2016) with information from four reanalysis products. This  
 221 includes the MERRA-2, Navy Aerosol Analysis and Prediction System (NAAPS), Japanese Reanalysis for Aerosol  
 222 (JRAero), and Copernicus Atmosphere Monitoring Service interim ReAnalysis (CAMSiRA) (Adebisi et al., 2020).  
 223 The aerosol RE of mineral dust strongly depends on both the magnitude of dust load and the dust size distribution  
 224 (Tegen and Lacis, 1996; Liao and Seinfeld, 1998). The DustCOMM data set contains total column loading ( $X, Y$ ) and  
 225 concentration of mineral dust resolved by season ( $T$ ) and particle size ( $S$ ) (Adebisi et al., 2020). To correct the bias in  
 226 the seasonally averaged size-resolved dust emission in the IMPACT model,  $E_{\text{IMPACT}}(X, Y, T, S)$ , the sum of bin 1, bin  
 227 2, and bin 3 dust emission flux was scaled by the seasonal mean of the ratio of the sum of bin 1, bin 2, and bin 3 dust  
 228 column loading between the model,  $L_{\text{IMPACT}}(X, Y, T, S)$ , and DustCOMM,  $L_{\text{DustCOMM}}(X, Y, T, S)$ , at each 2-D grid  
 229 box. The bias correction factor,  $L_{\text{bias}}(X, Y, T)$ , between the IMPACT model and DustCOMM data set is given by:

$$230 \quad L_{\text{bias}}(X, Y, T) = \sum_{S=1}^3 L_{\text{DustCOMM}}(X, Y, T, S) \div \sum_{S=1}^3 L_{\text{IMPACT}}(X, Y, T, S) \quad (1).$$

231 When the source function was used for high-latitude dust in the Northern Hemisphere, this led to substantially high  
 232 emissions and thus RE over there, likely due to the influences from long-range transported dust. Therefore, the direct  
 233 emissions of dust from the nine major source regions only (Kok et al., 2021) were adjusted using the DustCOMM  
 234 data (Fig. 1). To adjust the size bias in dust emissions, the mass fraction of emitted dust for each bin was prescribed  
 235 according to the size-resolved total column loading of DustCOMM at each 2-D grid box. The mass fraction for each  
 236 size bin,  $S_{\text{DustCOMM}}(X, Y, T, S)$  is given by:

$$237 \quad S_{\text{DustCOMM}}(X, Y, T, S) = L_{\text{DustCOMM}}(X, Y, T, S) \div \sum_{S=1}^4 L_{\text{DustCOMM}}(X, Y, T, S) \quad (2).$$

238 Thus, the dust emission flux after the adjustment,  $E_{\text{DustCOMM}}(X, Y, T, S)$  is given by:

$$239 \quad E_{\text{DustCOMM}}(X, Y, T, S) = L_{\text{bias}}(X, Y, T) \times S_{\text{DustCOMM}}(X, Y, T, S) \times E_{\text{IMPACT}}(X, Y, T) \quad (3).$$

240 Overall, the IMPACT-simulated lifetime of the dust aerosol for the second-size bin (7.8 days 1.26–2.5  $\mu\text{m}$  of diameter)  
 241 was in good agreement with the ensemble of model results ( $8.5 \pm 1.1$  days for the mass mean diameter of 1.8  $\mu\text{m}$ )  
 242 (Kok et al., 2017). To correct the bias in the seasonally averaged 3-D dust size distribution after the transport, the mass  
 243 fraction of dust concentration for each bin between 0.2 and 20.0  $\mu\text{m}$  of diameter was scaled at each 3-D grid box prior  
 244 to calculating the radiative fluxes using the RRTMG by the ratio of mass concentration of  $\text{PM}_{2.5}$  (i.e., the sum of bin  
 245 1 and bin 2) to each bin (Table 3).



## 246 **2.4 Asphericity factor for optical properties and sensitivity experiments to particle shape**

247 To account for the dust asphericity, an adjustment factor was applied to the spherical optical properties at each  
248 dust size parameter and refractive index. The adjustment factors for the spectral optical properties of non-spherical  
249 particles were calculated after Huang et al. (2021). The atmospheric aging of mineral dust can form a uniform coating  
250 around the mineral core and therefore decrease particle asphericity during transport. This is implicitly considered in  
251 the globally averaged shape distribution of dust (Huang et al., 2019). Specifically, Huang et al. (2021) combined  
252 globally representative dust shape distributions (Huang et al., 2020) with a shape-resolved single-scattering database  
253 (Meng et al., 2010). This database combines four computational methods (Mie theory, T-matrix method, discrete  
254 dipole approximation, and an improved geometric optics method) to compute the single-scattering properties of non-  
255 spherical dust for a wide range of shape descriptors. Huang et al. (2021) provided the look-up table containing optical  
256 properties of non-spherical dust as functions of size parameter and refractive index.

257 The approximation of particles to spheres is evaluated by applying aspherical factors to the optical properties  
258 of the mass extinction coefficient, single scattering albedo, and asymmetry parameter for SW, as well as absorption  
259 fraction of extinction for the LW. At the same time, we maintained the consideration of asphericity on the gravitational  
260 velocity and kept the dust concentrations unaltered between the spherical (denoted as “Sphere”) and aspherical  
261 (denoted as “Asphere”) cases.

## 262 **2.5 Spectral refractive index and sensitivity experiments to mineralogical compositions**

263 The aerosol RE of mineral dust depends on mineralogical composition. For the sensitivity simulation to the  
264 SW and LW refractive indices, we used the global mean of laboratory measurements of the refractive index from 19  
265 natural soils from various source regions around the world in Di Biagio et al. (2019) (denoted as “DB19”) and in Di  
266 Biagio et al. (2017) (denoted as “DB17”), respectively. To illustrate the regional heterogeneity of refractive index, the  
267 refractive index obtained from 19 samples was aggregated into 9 main source regions, and the arithmetic mean was  
268 calculated for each source region (Di Biagio et al., 2017, 2019). The regionally averaged imaginary parts of the  
269 refractive indices at the wavelength of 0.52  $\mu\text{m}$  and 9.7  $\mu\text{m}$  showed large differences in SW and LW absorptivity,  
270 respectively, between different samples collected at various geographical locations (Fig. 1).

271 The optical properties from the measurements for dust samples generated from 19 natural soils suggested a  
272 considerable role of Fe oxides in determining the SW absorption (Di Biagio et al., 2019). The refractive indices for  
273 mineral components were used for hematite, goethite (Bedidi and Cervelle, 1993), silicate particle group, quartz,  
274 gypsum ( $\text{CaSO}_4$ ) (Stegmann & Yang, 2017), and calcite ( $\text{CaCO}_3$ ) (Long et al., 1993) in the simulations denoted as  
275 “Mineral”. The hematite and goethite were treated separately according to the mineralogical map (Journet et al., 2014).

276 Consequently, hematite mass content averaged in the dust at emission (0.79% for fine and 0.50% for coarse from the  
277 IMPACT simulation) was lower than goethite content (1.8% and 1.3%, respectively) on a global scale. In addition to  
278 the primary emission of gypsum,  $\text{CaSO}_4$  is secondarily formed due to the dissolution/precipitation of  $\text{CaCO}_3$  in  
279 thermodynamic equilibrium condition (Ito and Feng, 2010). To illustrate the difference in refractive index, the global  
280 mean of the mineral composition was used for the comparison with DB19 (Fig. 1). The imaginary parts of the  
281 refractive indices from mineralogical map were higher than DB19, resulting in a stronger absorption over the SW  
282 spectrum.

283 The mineral dust LW refractive index also depends on its mineralogical composition (Sokolik et al., 1998; Di  
284 Biagio et al., 2017). The LW refractive index of Volz (1983) has been widely used in climate models and satellite  
285 remote sensing algorithms and thus was examined here (denoted as “V83”) (Song et al., 2018). The imaginary parts  
286 of the refractive indices from V83 were higher than DB17, resulting in a stronger absorption over most of the LW  
287 spectrum. To analyze the dependence of the results on less (more) absorptive SW and less (more) absorptive LW  
288 refractive indices, we made further sensitivity simulations by varying the values of imaginary parts of the refractive  
289 index within the range of values from Di Biagio et al. (2017, 2019) (10% or 90% percentiles for SW or LW,  
290 respectively) (denoted as “Less” or “More”). The associated real parts with 10% or 90% percentile imaginary parts  
291 for LW were calculated to account for the Kramers-Kronig relation (Lucarini et al., 2005).

## 292 **2.6 Semi-observationally-based dust SW and LW radiative effect efficiency**

293 To estimate dust radiative effect efficiency, aerosol and radiation remote sensing products have been used with  
294 various methods (Table 4) (Zhang and Christopher 2003; Li et al. 2004; Christopher and Jones 2007; Brindley and  
295 Russell 2009; Yang et al. 2009; Di Biagio et al. 2010; Hansell et al. 2010; Hansell et al. 2012; Song et al. 2018).

296 The instantaneous SW radiative effect efficiency at TOA is obtained from the linear regression of TOA  
297 radiation flux versus AOD observations, although the values in low-dust periods can be substantially influenced by  
298 other types of aerosols such as biomass burning (Li et al. 2004). This radiative effect efficiency corresponds to the  
299 instantaneous value derived under the limited condition at the measurements (e.g., solar position, atmospheric  
300 condition). From the extrapolation of the instantaneous value, the diurnal mean dust SW radiative effect efficiency at  
301 the surface and TOA can be derived based on model calculations.

302 The LW radiative effect efficiency at TOA can be obtained from the linear regression of TOA radiation flux  
303 versus AOD observations over the source regions (Brindley and Russell 2009). However, the observed outgoing LW  
304 radiation is not only dependent on DAOD but also on other factors such as dust layer height, water vapor content, and  
305 other types of aerosols. Thus, the LW radiative effect efficiency is estimated from the difference between observed

306 outgoing LW radiation and the dust-free outgoing LW radiation, which can be estimated using radiative transfer model  
307 (Song et al., 2018).

308 Consequently, the semi-observationally-based estimates of the dust radiative effect efficiency could be biased,  
309 in part, due to large uncertainties associated with the estimation method, the selection of cloud-free and dust-dominant  
310 data, and dust physicochemical properties. To understand the sensitivity of the dust radiative effect efficiency to the  
311 particle size distribution, asphericity, and refractive index of dust, radiative transfer computations have been carried  
312 out in previous studies (Li et al., 2004; Song et al., 2018). Song et al. (2018) found that the combination of the coarser  
313 dust particle size distribution and the more absorptive LW refractive index (V83) yielded the best simulation of the  
314 dust LW radiative effect in comparison with the satellite flux observations (i.e., Clouds and the Earth's Radiant Energy  
315 System (CERES)), compared to the less absorptive LW refractive index (DB17).

### 316 **3. Results and Discussions**

317 We evaluate our results from the sensitivity simulations against semi-observationally-based estimates of  
318  $DAOD_{550}$  in section 3.1 and radiative effect efficiency for SW and LW in section 3.2 and section 3.3, respectively.  
319 We focus this evaluation on the North Africa and the North Atlantic in boreal summer (June, July, and August) partly  
320 because that is the region and season for which most observational constraints on dust radiative effects are available.  
321 The better agreement is obtained for the less absorptive SW (Di Biagio et al., 2019) and the more absorptive LW  
322 (Volz, 1983) dust refractive indices with adjustments of size-resolved dust concentration and particle shape. Our  
323 improved simulation from IMPACT-Sphere-Mineral-V83 (E1) to DustCOMM-Asphere-DB19-V83 (E2)  
324 substantially reduces the model estimates of atmospheric radiative heating by mineral dust near the major source  
325 regions even though it induces only a minor difference in RE at TOA on a global scale (section 3.4). To elucidate the  
326 differences in dust radiative effects between different simulations, the results from the sensitivity simulations in  
327 conjunction with previous modeling studies are analyzed in section 3.5.

#### 328 **3.1 Dust load and aerosol optical depth**

329 We compared our model estimates of  $DAOD_{550}$  against semi-observationally-based data in box plots and  
330 Taylor diagrams (Taylor, 2001) for the evaluation of the various model experiments against semi-observationally-  
331 based estimates (Ridley et al., 2016; Adebisi et al., 2020) to provide a concise statistical summary of the bias,  
332 correlation coefficient, root mean square errors, and the ratio of standard deviation (Fig. 2, Tables S1 and S2).  
333 IMPACT-Sphere-Mineral-V83 (E1) simulations resulted in a significant underestimation of the global and annual  
334 mean of  $DAOD_{550}$  (0.023) (Fig. 2 and Table 3). After considering the dust asphericity for spectral optical properties,  
335 we adjusted IMPACT-simulated dust loads against the constraints on dust load from the DustCOMM data set. This

336 adjustment led the simulated total dust load to increase from 25 Tg (E1) to 32 Tg (E2), which addressed the issue of  
337 coarse dust underestimation and fine dust overestimation by the model (Fig. 3, Table 3). Consequently, the global and  
338 annual mean of DAOD<sub>550</sub> from DustCOMM-Asphere-DB19-V83 (E2) simulation (0.029) fell within the range in the  
339 semi-observationally-based estimate ( $0.030 \pm 0.005$ ) (Ridley et al., 2016) (Table 3). We found that the agreement in  
340 the median with the semi-observationally-based estimate (0.127) was improved from IMPACT-Sphere-Mineral-DB17  
341 (0.049) to DustCOMM-Asphere-DB19-V83 (0.117) (solid line within the box mark in Fig. 2d). We also found higher  
342 DAOD<sub>550</sub> from E2 than E1 over East Asia and Bodele/Sudan in winter (Fig. 2, Table S2). The better agreement  
343 suggested that DustCOMM-Asphere-DB19-V83 (E2) simulation was reasonably constrained by the DAOD<sub>550</sub> (Ridley  
344 et al., 2016; Adebisi et al., 2020).

### 345 **3.2 Dust SW radiative effect efficiency**

346 Modeled estimates of clear-sky dust SW radiative effect efficiencies ( $\text{W} \cdot \text{m}^{-2} \text{DAOD}_{550}^{-1}$ ) at the surface (Table  
347 S3) and TOA (Table S4) were compared with estimates reported by regional studies based on satellite observations  
348 over the North Africa and the North Atlantic (Fig. 4). Sensitivity simulations demonstrated that the radiative effect  
349 efficiency strongly depended on the particle size, refractive index, and particle shape (Fig. 4). The adjustment of size-  
350 resolved dust concentration and shape with the same refractive index led to overestimates of the SW radiative effect  
351 efficiencies against semi-observationally-based data at TOA (from E1 to E6 in Fig. 4h), because coarser dust absorbs  
352 more SW radiation efficiently than finer particles. Subsequently, the use of less absorptive SW refractive index with  
353 DustCOMM-Asphere-DB19-V83 (E2) simulations led to a better agreement (from E6 to E2 in Fig. 4). On the other  
354 hand, the use of much less (10% percentile) absorptive SW refractive index from DustCOMM-Asphere-Less-More  
355 (E7) simulation deteriorated the agreement due to the underestimate of cooling at the surface (Fig. 4g). In contrast,  
356 the use of a more absorptive SW refractive index from DustCOMM-Asphere-Mineral-V83 (E6) improved the  
357 agreement at the surface. However, the semi-observationally-based estimates of diurnally averaged radiative effect  
358 efficiency at the surface were derived from extrapolation of the instantaneous values, which would affect the  
359 comparison due to differences in the methodologies between dust models (section 2.6). The differences in the model-  
360 based estimates of radiative effect efficiency might arise from different data sets of the refractive index, size  
361 distribution, and particle shape (Song et al., 2018).

### 362 **3.3 Dust LW radiative effect efficiency**

363 Modeled estimates of clear-sky dust LW (Fig. 5) radiative effect efficiencies ( $\text{W} \cdot \text{m}^{-2} \text{DAOD}_{550}^{-1}$ ) at the surface  
364 (Table S5) and TOA (Table S6) were compared with estimates reported by regional studies based on satellite

365 observations over North Africa and the North Atlantic. Sensitivity simulations demonstrated that the radiative effect  
366 efficiency strongly depended on the particle size, refractive index, and particle shape (Fig. 5). Both the IMPACT-  
367 Sphere-Mineral-V83 (E1) and DustCOMM-Asphere-DB19-V83 (E2) simulations yielded better agreement with semi-  
368 observationally-based data at the surface and TOA, compared to the less absorptive LW dust refractive indices (E3,  
369 E4, E5, and E7) (Fig. 5). The relatively high LW radiative effect efficiencies over western Africa were also consistent  
370 with the semi-observationally-based data. On the other hand, the relatively low LW radiative effect efficiencies were  
371 found over eastern Africa. Moving toward the northeastern side of the region, however, the associated uncertainties  
372 in the semi-observationally-based values increased (Brindley and Russell 2009). The dust LW radiative effect  
373 efficiency depends strongly on the vertical profile of dust concentration, temperature, and water vapor, which would  
374 affect the comparison due to a high variability in these factors (section 2.6).

### 375 **3.4 Less atmospheric radiative heating by dust due to the synergy of coarser size and aspherical shape**

376 The Saharan dust cools the ground surface by reducing the solar radiation reaching the surface and warms the  
377 atmosphere by absorbing solar radiation (Fig. 6). On the other hand, thermal emission by dust warms the surface and  
378 cools the atmosphere (Fig. 7). Our sensitivity simulations showed that the annually averaged net instantaneous  
379 radiative effect due to mineral aerosol (NET) ranged from  $-0.48$  (DustCOMM-Asphere-Less-Less) to  $+0.25$   
380 (DustCOMM-Asphere-Mineral-V83)  $\text{W}\cdot\text{m}^{-2}$  at TOA (Table 5). The net RE from both the IMPACT-Sphere-Mineral-  
381 V83 ( $-0.00 \text{ W}\cdot\text{m}^{-2}$ ) and DustCOMM-Asphere-DB19-V83 ( $-0.08 \text{ W}\cdot\text{m}^{-2}$ ) simulations resulted within 98%  
382 confidential interval of DustCOMM data set ( $-0.27$  to  $0.14 \text{ W}\cdot\text{m}^{-2}$ ).

383 The SW RE by dust outweighs the LW warming effect at the surface in the IMPACT-Sphere-Mineral-V83  
384 (E1) simulation (Fig. 8). Consequently, the highly absorbing dust could play an important role in the aerosol radiative  
385 forcing for the climate models to alter the West African monsoon, with the radiative heating concentrated in the dust  
386 layer (Miller et al., 2004b; Lau et al., 2009). Our model results of dust RE from DustCOMM-Asphere-DB19-V83  
387 (E2) simulation, however, suggested that the surface warming was substantially enhanced near the strong dust source  
388 regions ( $-0.23 \text{ W}\cdot\text{m}^{-2}$  on a global scale) (Fig. 8), compared to the IMPACT-Sphere-Mineral-V83 simulation ( $-0.60$   
389  $\text{W}\cdot\text{m}^{-2}$  on a global scale). Thus, our results demonstrated that the atmospheric radiative heating by mineral dust was  
390 substantially reduced for DustCOMM-Asphere-DB19-V83 (E2) simulation ( $0.15 \text{ W}\cdot\text{m}^{-2}$ ), compared to the IMPACT-  
391 Sphere-Mineral-V83 (E1) simulation ( $0.59 \text{ W}\cdot\text{m}^{-2}$ ).

### 392 3.5 Variability of dust radiative effect in different simulations

393 To elucidate the differences in dust radiative effects between the IMPACT-Sphere-Mineral-V83 (E1) and  
394 DustCOMM-Asphere-DB19-V83 (E2) simulations and to explore the variability in different previous model estimates  
395 (Fig. 9), the differences in annually averaged radiative effects of mineral dust from DustCOMM-Asphere-DB19-  
396 DB17 (E4) simulation were shown in Fig. 10. A slope of one in Fig. 10 represented an identical change in both the  
397 surface and TOA and thus corresponded to no change in radiative heating within the atmosphere. The distances from  
398 the DustCOMM-Asphere-DB19-DB17 (E4) simulation demonstrated that large uncertainties existed for the size  
399 distribution and spectral optical properties. Our sensitivity simulations revealed that the DustCOMM-Asphere-DB19-  
400 V83 (E2) simulation led to a similar net RE at TOA to the IMPACT-Sphere-Mineral-V83 (E1) simulation but resulted  
401 in less cooling at the surface (Fig. 9). This revision can be divided into (1) the size-resolved abundance (black  
402 hexagons, E3 – E4, in Fig. 10), (2) SW refractive index (red diamonds, E6 – E4, in Fig. 10), and (3) particle shape  
403 (red circles, E5– E4, in Fig. 10). Additionally, we show the sensitivity of dust RE to LW refractive index (DB17),  
404 which was used by both Di Biagio et al. (2020) and Balkanski et al. (2021).

405 First, at TOA, the SW RE was more sensitive to the size-resolved abundance ( $-0.17 \text{ W}\cdot\text{m}^{-2}$  at the vertical axis  
406 of black hexagon in Fig. 10a), compared to LW ( $0.00 \text{ W}\cdot\text{m}^{-2}$  at the vertical axis of black hexagon in Fig. 10b). Second,  
407 this less SW cooling effect with coarser dust (E3 – E4) was partially compensated for by more SW cooling with the  
408 use of the less absorptive SW refractive index (E4:  $-0.32 \text{ W}\cdot\text{m}^{-2}$ ) than E6 ( $0.02 \text{ W}\cdot\text{m}^{-2}$ ). Thirdly, the sensitivity of  
409 SW RE to dust asphericity was rather minor ( $0.04 \text{ W}\cdot\text{m}^{-2}$  at the vertical axis of red circle in Fig. 10a), partly because  
410 the lower DAOD was compensated for by the lower asymmetry parameter of spherical dust, which enhanced the  
411 amount of radiation scattered backward to space (Räisänen et al., 2013; Colarco et al., 2014). The partial compensation  
412 led to a small enhancement of SW RE for the IMPACT-Sphere-Mineral-V83 (E1) simulation and thus the resulting  
413 similar net RE to DustCOMM-Asphere-DB19-V83 (E2) at TOA (Fig. 9).

414 In contrast, at the surface, our sensitivity simulations demonstrated substantially different responses in the RE,  
415 mostly because of LW warming effects (Fig. 9). The enhanced LW warming by coarser dust ( $-0.08 \text{ W}\cdot\text{m}^{-2}$  at the  
416 horizontal axis of black hexagon in Fig. 10b) was accompanied by the asphericity ( $-0.15 \text{ W}\cdot\text{m}^{-2}$  at the horizontal axis  
417 of red circle in Fig. 10b), because the enhancement of the absorption fraction of extinction due to asphericity was  
418 larger at coarser size. The enhanced LW warming effects of each as well as the synergy was further amplified using  
419 the more absorptive LW dust refractive index (Volz, 1983) (at the horizontal axis of red diamond in Fig. 10b). As a  
420 result, our sensitivity simulations revealed that substantially less dust absorption at LW due to the underestimation of  
421 the coarse dust load and the assumption of the spherical shape (IMPACT-Sphere-Mineral-V83) contributed to the less  
422 surface warming, compared to DustCOMM-Asphere-DB19-V83 (Fig. 9).

423 A relatively good agreement of net RE by dust at TOA with both Di Biagio et al. (2020) ( $-0.06 \text{ W}\cdot\text{m}^{-2}$ ) and  
424 Balkanski et al. (2021) ( $-0.02 \text{ W}\cdot\text{m}^{-2}$ ) could be obtained from both the IMPACT-Sphere-Mineral-V83 (E1:  $-0.00$   
425  $\text{W}\cdot\text{m}^{-2}$ ) and DustCOMM-Asphere-DB19-V83 (E2:  $-0.08 \text{ W}\cdot\text{m}^{-2}$ ) simulations (Fig. 9 and Table 5). On the other hand,  
426 our modeled dust net RE at the surface from DustCOMM-Asphere-DB19-V83 (E2:  $-0.23 \text{ W}\cdot\text{m}^{-2}$ ) indicated much  
427 less cooling than Di Biagio et al. (2020) ( $-0.63 \text{ W}\cdot\text{m}^{-2}$ ), Balkanski et al. (2021) ( $-1.01 \text{ W}\cdot\text{m}^{-2}$ ), and IMPACT-Sphere-  
428 Mineral-V83 (E1:  $-0.60 \text{ W}\cdot\text{m}^{-2}$ ). The synergy of coarser size and aspherical dust could contribute to the less surface  
429 cooling of the DustCOMM-Asphere-DB19-V83 (E2), because of enhanced LW warming. At the same time, both Di  
430 Biagio et al. (2020) and Balkanski et al. (2021) used DB17 and considered dust with diameters more than  $20 \mu\text{m}$ .  
431 Thus, the more absorptive LW dust refractive index (V83, E6 for LW:  $1.00 \text{ W}\cdot\text{m}^{-2}$ ) than DB17 (E4 for LW:  $0.58$   
432  $\text{W}\cdot\text{m}^{-2}$ ) (E6 – E4 for LW:  $0.42 \text{ W}\cdot\text{m}^{-2}$  at the horizontal axis of red diamond in Fig. 10b) could also contribute to the  
433 less surface cooling, which might be partially compensated for in our model by the omission of dust with diameters  
434 more than  $20 \mu\text{m}$ . Consequently, our estimate of atmospheric radiative heating by dust from DustCOMM-Asphere-  
435 DB19-V83 (E2:  $0.15 \text{ W}\cdot\text{m}^{-2}$ ) was lower than Di Biagio et al. (2020) ( $0.63 \text{ W}\cdot\text{m}^{-2}$ ), Balkanski et al. (2021) ( $0.98$   
436  $\text{W}\cdot\text{m}^{-2}$ ), and IMPACT-Sphere-Mineral-V83 (E1:  $0.59 \text{ W}\cdot\text{m}^{-2}$ ). Additionally, the hot and dry climate over brighter  
437 desert surface exaggerates differences in RE at the surface between the models (Miller et al., 2014). The low humidity  
438 allows dust particles to absorb LW radiation with reduced competition from water vapor, while high temperatures  
439 within the boundary layer increase downward thermal emission by dust (Liao and Seinfeld, 1998). The reduction of  
440 fine dust load after the adjustment leads to underestimates of the SW cooling at TOA. To improve agreement against  
441 semi-observationally-based estimate of the radiative effect efficiency at TOA, the less absorptive SW dust refractive  
442 index is required for coarser aspherical dust. Thus, uncertainties in the size-resolved dust concentration, particle shape,  
443 and refractive index contribute to the diversity in the simulated dust RE at the surface.

#### 444 4. Conclusions

445 Accurate estimates of the size-resolved dust abundance, their spectral optical properties, and their seasonality  
446 in regional and vertical scales provide a step towards a more reliable projection of the climatic feedback of mineral  
447 aerosols. The radiative effect efficiency depends on numerous variables in model simulations, including the spatial  
448 distribution and temporal variation of size-resolved dust concentrations, the mass extinction coefficient, single  
449 scattering albedo, and asymmetry parameter of dust. Since the models typically underestimate the coarse dust load  
450 and overestimate the fine dust load, the sensitivity to the aerosol absorptivity might be considerably different from  
451 previous studies. Thus, the model results should be re-evaluated against semi-observationally-based estimate of the  
452  $\text{DAOD}_{550}$  and dust radiative effect efficiency.

453 We improved the accuracy of the simulations by adjusting the bias in size-resolved aspherical dust  
454 concentration with the DustCOMM data set. Alternatively, dust mineralogy might contribute to the underestimation  
455 of modeled aerosol absorption compared to satellite observations (Lacagnina et al., 2015). This enhanced aerosol  
456 absorption was examined by specifying the mineralogy with varying amounts of light-absorbing Fe oxides for SW.  
457 The better agreement with the semi-observationally-based data of dust radiative effect efficiency was obtained using  
458 the less absorptive SW dust refractive indices after the adjustments of dust sizes and shapes.

459 The diversity of modeled dust net RE at the surface ( $-1.64 \text{ W}\cdot\text{m}^{-2}$  to  $-0.20 \text{ W}\cdot\text{m}^{-2}$ ) is much larger than at TOA  
460 ( $-0.01 \text{ W}\cdot\text{m}^{-2}$  to  $-0.60 \text{ W}\cdot\text{m}^{-2}$ ), partly because the refractive index is optimized to obtain reasonable agreement against  
461 satellite observations of TOA radiation flux (e.g., CERES). The uncertainties in the size-resolved dust concentration,  
462 particle shape, and refractive index contribute to the model diversity at the surface. DustCOMM-Asphere-DB19-V83  
463 (E2) simulation resulted in less cooling at the surface by the synergy of coarser size and aspherical shape, compared  
464 to IMPACT-Sphere-Mineral-V83 (E1) simulation ( $-0.23$  vs.  $-0.60 \text{ W}\cdot\text{m}^{-2}$  on a global scale). Consequently, the  
465 atmospheric heating due to mineral dust was substantially reduced for the DustCOMM-Asphere-DB19-V83 (E2)  
466 simulation ( $0.15 \text{ W}\cdot\text{m}^{-2}$ ), compared to the intensified atmospheric heating from the IMPACT-Sphere-Mineral-V83  
467 (E1) simulation ( $0.59 \text{ W}\cdot\text{m}^{-2}$ ). The less intensified atmospheric heating due to mineral dust could substantially modify  
468 the vertical temperature profile in Earth system models and thus has important implications for the projection of dust  
469 feedback near the major source regions in the past and future climate changes (Kok et al., 2018). More accurate  
470 estimates of semi-observationally-based dust SW and LW radiative effect efficiencies over strong dust source regions  
471 are needed to narrow the uncertainty in the RE.

472 Currently, the model did not include dust particles above  $20 \mu\text{m}$ , but a substantial fraction of airborne dust near  
473 source regions may be above this threshold (Ryder et al., 2019). Moreover, such large particles can be transported to  
474 higher altitudes and longer distances than the model prediction. The higher the dust layer resides, the larger the dust  
475 LW RE at TOA is estimated under the clear-sky conditions (Liao and Seinfeld, 1998). Marine sediment traps, which  
476 are located underneath the main Saharan dust plume in the Atlantic Ocean, suggest that giant particles are dominated  
477 by platy mica and rounded quartz particles (van der Does et al., 2016). Thus, mineral composition of the giant particles  
478 could be different from the aerosol samples generated from soils in the laboratory by Di Biagio et al. (2017), which  
479 may reflect less absorbing LW refractive index of DB17 than V83. Indeed, the dust sample was collected for V83  
480 from rainwater after strong wind. On the other hand, the contribution of the LW scattering might be underestimated  
481 in the models, as Di Biagio et al. (2020) noted that the adjustment factor was estimated for dust of diameter less than  
482  $10 \mu\text{m}$  and thus might be a lower approximation of the LW scattering by coarse dust. Therefore, a better understanding  
483 of the effect of such large particles beyond  $20 \mu\text{m}$  and mineralogical composition on radiation balance remains a topic



484 of active research, given their potential to amplify the warming of the climate system. In such an extreme case as the  
485 “Godzilla” dust storm over the North Africa and the tropical Atlantic in June 2020 (Francis et al., 2020), the dust  
486 loading could be larger than that examined for this study, and our estimates of the warming effects might be  
487 conservative during such events. However, to keep the giant particles in the atmosphere, the modeled deposition fluxes  
488 should be reduced from the current model. Therefore, models should improve their ability to capture the evolution of  
489 the dust size distribution as the plumes move downwind of the source regions.

#### 490 **Code availability.**

491 The source code of the RRTMG has been obtained from the website at [https://github.com/AER-RC/RRTMG\\_LW](https://github.com/AER-RC/RRTMG_LW) and  
492 [https://github.com/AER-RC/RRTMG\\_SW](https://github.com/AER-RC/RRTMG_SW). The source code of the Kramers-Kronig relations has been obtained from  
493 the website at [https://www.mathworks.com/matlabcentral/fileexchange/8135-tools-for-data-analysis-in-optics-  
494 acoustics-signal-processing](https://www.mathworks.com/matlabcentral/fileexchange/8135-tools-for-data-analysis-in-optics-acoustics-signal-processing). The source code of the Taylor diagram has been obtained from the web site at  
495 <https://www.mathworks.com/matlabcentral/fileexchange/20559-taylor-diagram>.

#### 496 **Data availability.**

497 SMAP data have been obtained from the website at <https://nsidc.org/data/smap/smap-data.html>. MODIS land data  
498 have been retrieved from the website at <https://ladsweb.modaps.eosdis.nasa.gov/>. MERRA-2 data have been provided  
499 by the Global Modeling and Assimilation Office (GMAO) at NASA Goddard Space Flight Center  
500 (<https://disc.gsfc.nasa.gov/datasets/>). The DustCOMM data are available at <https://dustcomm.atmos.ucla.edu/>. The  
501 datasets supporting the conclusions of this article are included within the article and its supplement file.

#### 502 **Supplement.**

503 The supplement related to this article is available online at:

#### 504 **Author contributions.**

505 AI and JFK initiated the modeling collaboration with semi-observationally-based data sets. AI carried out the  
506 modeling study. AAA, YH, JFK contributed semi-observationally-based data sets of DustCOMM and asphericity  
507 factor. All authors read and approved the final manuscript.

#### 508 **Competing interests.**

509 The authors declare that they have no competing interests.

510 **Acknowledgements.**

511 Numerical simulations were performed using the Hewlett Packard Enterprise (HPE) Apollo at the Japan Agency for  
512 Marine-Earth Science and Technology (JAMSTEC).

513 **Financial support.**

514 Support for this research was provided to A.I. by JSPS KAKENHI Grant Number 20H04329 and 18H04143, and  
515 Integrated Research Program for Advancing Climate Models (TOUGOU) Grant Number JPMXD0717935715 from  
516 the Ministry of Education, Culture, Sports, Science and Technology (MEXT), Japan. This work was developed with  
517 support from the University of California President's Postdoctoral Fellowship awarded to A.A.A., and from the  
518 National Science Foundation (NSF) grants 1552519 and 1856389 awarded to J.F.K. Y.H. acknowledges support from  
519 NASA grant 80NSSC19K1346, awarded under the Future Investigators in NASA Earth and Space Science and  
520 Technology (FINESST) program.

521 **Review statement.**

522 This paper was edited by Susannah Burrows and reviewed by four anonymous referees.

523 **References**

- 524 Adebisi, A. A., Kok, J. F., Wang, Y., Ito, A., Ridley, D. A., Nabat, P., and Zhao, C.: Dust Constraints from joint  
525 Observational-Modelling-experiMental analysis (DustCOMM): comparison with measurements and model  
526 simulations, *Atmos. Chem. Phys.*, 20, 829–863, <https://doi.org/10.5194/acp-20-829-2020>, 2020.
- 527 Adebisi, A. A. and Kok, J. F.: Climate models miss most of the coarse dust in the atmosphere, *Sci. Adv.*, 6, eaaz9507,  
528 <https://doi.org/10.1126/sciadv.aaz9507>, 2020.
- 529 Al-Abadleh, H. A.: Aging of atmospheric aerosols and the role of iron in catalyzing brown carbon formation. *Environ.*  
530 *Sci.: Atmos.*, 1, 297–345, <https://doi.org/10.1039/D1EA00038A>, 2021.
- 531 Albani, S., Mahowald, N. M., Perry, A. T., Scanza, R. A., Heavens, N. G., Zender, C. S., Maggi, V., Kok, J. F., and  
532 Otto-Bliesner, B. L.: Improved dust representation in the Community Atmosphere Model. *J. Adv. Model.*  
533 *Earth Syst.*, 6, 541–570, <https://doi.org/10.1002/2013MS000279>, 2014.
- 534 Ansmann, A., Rittmeister, F., Engelmann, R., Basart, S., Jorba, O., Spyrou, C., Remy, S., Skupin, A., Baars, H., Seifert,  
535 P., Senf, F., and Kanitz, T.: Profiling of Saharan dust from the Caribbean to western Africa – Part 2:  
536 Shipborne lidar measurements versus forecasts, *Atmos. Chem. Phys.*, 17, 14987–15006,  
537 <https://doi.org/10.5194/acp-17-14987-2017>, 2017.

538 Balkanski, Y., Schulz, M., Claquin, T., and Guibert, S.: Reevaluation of Mineral aerosol radiative forcings suggests a  
539 better agreement with satellite and AERONET data, *Atmos. Chem. Phys.*, 7, 81–95,  
540 <https://doi.org/10.5194/acp-7-81-2007>, 2007.

541 Balkanski, Y., Bonnet, R., Boucher, O., Checa-Garcia, R., and Servonnat, J.: Better representation of dust can improve  
542 climate models with too weak an African monsoon, *Atmos. Chem. Phys.*, 21, 11423–11435,  
543 <https://doi.org/10.5194/acp-21-11423-2021>, 2021.

544 Bedidi, A. and Cervelle, B.: Light scattering by spherical particles with hematite and goethitelike optical properties:  
545 effect of water impregnation, *J. Geophys. Res.*, 98, 11941–11952, 1993, <https://doi.org/10.1029/93JB00188>.

546 Brindley, H. E. and Russell, J. E.: An assessment of Saharan dust loading and the corresponding cloud-free longwave  
547 direct radiative effect from geostationary satellite observations, *J. Geophys. Res.-Atmos.*, 114, D23201,  
548 <https://doi.org/10.1029/2008jd011635>, 2009.

549 Colarco, P. R., Nowotnick, E. P., Randles, C. A., Yi, B. Q., Yang, P., Kim, K. M., Smith, J. A., and Bardeen, C. G.:  
550 Impact of radiatively interactive dust aerosols in the NASA GEOS-5 climate model: Sensitivity to dust  
551 particle shape and refractive index, *J. Geophys. Res.-Atmos.*, 119, 753–786,  
552 <https://doi.org/10.1002/2013JD020046>, 2014.

553 Christopher, S. A. and Jones, T.: Satellite-based assessment of cloud-free net radiative effect of dust aerosols over the  
554 Atlantic Ocean, *Geophys. Res. Lett.*, 34, L02810, doi:10.1029/2006GL027783, 2007.

555 Di Biagio, C., di Sarra, A., and Meloni, D.: Large atmospheric shortwave radiative forcing by Mediterranean aerosol  
556 derived from simultaneous ground-based and spaceborne observations, and dependence on the aerosol type  
557 and single scattering albedo, *J. Geophys. Res.*, 115, D10209, <https://doi.org/10.1029/2009JD012697>, 2010.

558 Di Biagio, C., Formenti, P., Balkanski, Y., Caponi, L., Cazaunau, M., Pangui, E., Journet, E., Nowak, S., Caquineau,  
559 S., Andreae, M. O., Kandler, K., Saeed, T., Piketh, S., Seibert, D., Williams, E., and Doussin, J.-F.: Global  
560 scale variability of the mineral dust long-wave refractive index: a new dataset of in situ measurements for  
561 climate modeling and remote sensing, *Atmos. Chem. Phys.*, 17, 1901–1929, [https://doi.org/10.5194/acp-17-](https://doi.org/10.5194/acp-17-1901-2017)  
562 1901-2017, 2017.

563 Di Biagio, C., Formenti, P., Balkanski, Y., Caponi, L., Cazaunau, M., Pangui, E., Journet, E., Nowak, S., Andreae, M.  
564 O., Kandler, K., Saeed, T., Piketh, S., Seibert, D., Williams, E., and Doussin, J.-F.: Complex refractive  
565 indices and single-scattering albedo of global dust aerosols in the shortwave spectrum and relationship to  
566 size and iron content, *Atmos. Chem. Phys.*, 19, 15503–15531, <https://doi.org/10.5194/acp-19-15503-2019>,  
567 2019.

568 Di Biagio, C., Balkanski, Y., Albani, S., Boucher, O., and Formenti, P.: Direct radiative effect by mineral dust aerosols  
569 constrained by new microphysical and spectral optical data. *Geophys. Res. Lett.*, 47, e2019GL086186,  
570 <https://doi.org/10.1029/2019GL086186>, 2020.

571 Dufresne, J., Gautier, C., Ricchizzi, P., and Fouquart, Y.: Longwave scattering effects of mineral aerosols, *J. Atmos.*  
572 *Sci.*, 59(12), 1959–1966, 2002, [https://doi.org/10.1175/1520-0469\(2002\)059<1959:LSEOMA>2.0.CO;2](https://doi.org/10.1175/1520-0469(2002)059<1959:LSEOMA>2.0.CO;2).

573 Feng, Y. and Penner, J. E.: Global modeling of nitrate and ammonium: Interaction of aerosols and tropospheric  
574 chemistry, *J. Geophys. Res.*, 112, D01304, doi:10.1029/2005JD006404, 2007.

575 Francis, D., Fonseca, R., Nelli, N., Cuesta, J., Weston, M., Evan, A., and Temimi, M.: The atmospheric drivers of the  
576 major Saharan dust storm in June 2020. *Geophys. Res. Lett.*, 47, e2020GL090102,  
577 <https://doi.org/10.1029/2020GL090102>, 2020.

578 Friedl, M. and Sulla-Menashe, D.: MCD12Q1 MODIS/Terra+Aqua Land Cover Type Yearly L3 Global 500m SIN  
579 Grid V006 [Data set]. NASA EOSDIS Land Processes DAAC,  
580 <https://doi.org/10.5067/MODIS/MCD12Q1.006>, 2019.

581 Gelaro, R., McCarty, W., Suárez, M. J., Todling, R., Molod, A., Takacs, L., Randles, C. A., Darmenov, A., Bosilovich,  
582 M. G., Reichle, R., Wargan, K., Coy, L., Cullather, R., Draper, C., Akella, S., Buchard, V., Conaty, A., da  
583 Silva, A. M., Gu, W., Kim, G.-K., Koster, R., Lucchesi, R., Merkova, D., Nielsen, J. E., Partyka, G., Pawson,  
584 S., Putman, W., Rienecker, M., Schubert, S. D., Sienkiewicz, M., and Zhao, B.: The Modern-Era  
585 Retrospective Analysis for Research and Applications, Version 2 (MERRA-2), *J. Climate*, 30, 5419–5454  
586 <https://doi.org/10.1175/JCLI-D-16-0758.1>, 2017,.

587 Gettelman, A., Liu, X., Ghan, S. J., Morrison, H., Park, S., Conley, A. J., Klein, S. A., Boyle, J., Mitchell, D. L., and  
588 Li, J. L. F.: Global simulations of ice nucleation and ice supersaturation with an improved cloud scheme in  
589 the Community Atmosphere Model, *J. Geophys. Res.*, 115, D18216, <https://doi.org/10.1029/2009jd013797>,  
590 2010.

591 Harrison, R. G., Nicoll, K. A., Marlton, G. J., Ryder, C. L., and Bennett, A. J.: Saharan dust plume charging observed  
592 over the UK, *Environ. Res. Lett.*, 13, 054018, <https://doi.org/10.1088/1748-9326/aabcd9>, 2018.

593 Hansell, R. A., Tsay, S., Hsu, N. C., Ji, Q., Bell, S.W., Brent, N. H., Welton, E. J., Roush, T. L., Zhang, W., Huang,  
594 J., Li Z. Q., and Chen, H.: An assessment of the surface longwave direct radiative effect of airborne dust in  
595 Zhangye, China, during the Asian Monsoon Years field experiment (2008), *J. Geophys. Res.*, 117, D00K39,  
596 <https://doi.org/10.1029/2011JD017370>, 2012.

597 Hansell, R. A., Tsay, S. C., Ji, Q., Hsu, N. C., Jeong, M. J., Wang, S. H., Reid, J. S., Liou, K. N., and Ou, S. C.: An  
598 assessment of the surface longwave direct radiative effect of airborne saharan dust during the NAMMA field  
599 campaign, *J. Atmos. Sci.* 67, 1048–1065, doi:10.1175/2009JAS3257.1, 2010.

600 Heald, C. L., Ridley, D. A., Kroll, J. H., Barrett, S. R. H., Cady-Pereira, K. E., Alvarado, M. J., and Holmes, C. D.:  
601 Contrasting the direct radiative effect and direct radiative forcing of aerosols, *Atmos. Chem. Phys.*, 14, 5513–  
602 5527, <https://doi.org/10.5194/acp-14-5513-2014>, 2014.

603 Huang, Y., Kok, J. F., Kandler, K., Lindqvist, H., Nousiainen, T., Sakai, T., Adebisi, A., and Jokinen, O.: Climate  
604 Models and Remote Sensing Retrievals Neglect Substantial Desert Dust Asphericity, *Geophys. Res. Lett.*,  
605 47, e2019GL086592, <https://doi.org/10.1029/2019GL086592>, 2020.

606 Huang, Y., Adebisi, A. A., Formenti, P., and Kok, J. F.: Linking the different diameter types of aspherical desert dust  
607 indicates that models underestimate coarse dust emission, *Geophys. Res. Lett.*, 48, e2020GL092054,  
608 <https://doi.org/10.1029/2020GL092054>, 2021.

609 Hoshyaripour, G. A., Bachmann, V., Förstner, J., Steiner, A., Vogel, H., Wagner, F., Walter, C., and Vogel, B.: Effects  
610 of Particle Nonsphericity on Dust Optical Properties in a Forecast System: Implications for Model-  
611 Observation Comparison, *J. Geophys. Res.-Atmos.*, 124, 2018JD030228,  
612 <https://doi.org/10.1029/2018JD030228>, 2019.

613 Iacono, M. J., Delamere, J. S., Mlawer, E. J., Shephard, M. W., Clough, S. A., and Collins, W. D.: Radiative forcing  
614 by long-lived greenhouse gases: Calculations with the AER radiative transfer models, *J. Geophys. Res.*, 113,  
615 D13103, <https://doi.org/10.1029/2008JD009944>, 2008.

616 Ito, A. and Feng, Y.: Role of dust alkalinity in acid mobilization of iron, *Atmos. Chem. Phys.*, 10, 9237–9250,  
617 <https://doi.org/10.5194/acp-10-9237-2010>, 2010.

618 Ito, A. and Shi, Z.: Delivery of anthropogenic bioavailable iron from mineral dust and combustion aerosols to the  
619 ocean, *Atmos. Chem. Phys.*, 16, 85–99, <https://doi.org/10.5194/acp-16-85-2016>, 2016.

620 Ito, A. and Kok, J. F.: Do dust emissions from sparsely vegetated regions dominate atmospheric iron supply to the  
621 Southern Ocean?, *J. Geophys. Res.-Atmos.*, 122, 3987–4002, <https://doi.org/10.1002/2016JD025939>, 2017.

622 Ito, A., Lin, G., and Penner, J. E.: Radiative forcing by lightabsorbing aerosols of pyrogenetic iron oxides, *Sci. Rep.-*  
623 *UK*, 8, 7347, <https://doi.org/10.1038/s41598-018-25756-3>, 2018.

624 Ito, A., Myriokefalitakis, S., Kanakidou, M., Mahowald, N. M., Scanza, R. A., Hamilton, D. S., Baker, A. R., Jickells,  
625 T., Sarin, M., Bikkina, S., Gao, Y., Shelley, R. U., Buck, C. S., Landing, W. M., Bowie, A. R., Perron, M.,  
626 M. G., Guieu, C., Meskhidze, N., Johnson, M. S., Feng, Y., Kok, J. F., Nenes, A., and Duce, R. A.: Pyrogenic

627 iron: The missing link to high iron solubility in aerosols, *Sci. Adv.*, 5, eaau7671,  
628 <https://doi.org/10.1126/sciadv.aau7671>, 2019.

629 Ito, A., Perron, M. M. G., Proemse, B. C., Strzelec, M., Gault-Ringold, M., Boyd, P. W., and Bowie, A. R.: Evaluation  
630 of aerosol iron solubility over Australian coastal regions based on inverse modeling: implications of bushfires  
631 on bioaccessible iron concentrations in the Southern Hemisphere, *Prog. Earth Planet. Sci.*, 7, 42,  
632 <https://doi.org/10.1186/s40645-020-00357-9>, 2020.

633 Ito, A., Ye, Y., Baldo, C., and Shi, Z.: Ocean fertilization by pyrogenic aerosol iron, *npj Clim. Atmos. Sci.*, 4, 30,  
634 <https://doi.org/10.1038/s41612-021-00185-8>, 2021.

635 Journet, E., Balkanski, Y., and Harrison, S. P.: A new data set of soil mineralogy for dust-cycle modeling, *Atmos.*  
636 *Chem. Phys.*, 14, 3801–3816, <https://doi.org/10.5194/acp-14-3801-2014>, 2014.

637 Kok, J. F.: A scaling theory for the size distribution of emitted dust aerosols suggests climate models underestimate  
638 the size of the global dust cycle, *P. Natl. Acad. Sci. USA*, 108, 1016–1021,  
639 <https://doi.org/10.1073/pnas.1014798108>, 2011.

640 Kok, J. F., Parteli, E. J. R., Michaels, T. I., and Karam, D. B.: The physics of wind-blown sand and dust, *Rep. Prog.*  
641 *Phys.*, 75, 106901, doi:10.1088/0034-4885/75/10/106901, 2012.

642 Kok, J. F., Mahowald, N. M., Fratini, G., Gillies, J. A., Ishizuka, M., Leys, J. F., Mikami, M., Park, M.-S., Park, S.-  
643 U., Van Pelt, R. S., and Zobeck, T. M.: An improved dust emission model – Part 1: Model description and  
644 comparison against measurements, *Atmos. Chem. Phys.*, 14, 13023–13041, [https://doi.org/10.5194/acp-14-](https://doi.org/10.5194/acp-14-13023-2014)  
645 [13023-2014](https://doi.org/10.5194/acp-14-13023-2014), 2014.

646 Kok, J. F., Ridley, D. A., Zhou, Q., Miller, R. L., Zhao, C., Heald, C. L., Ward, D. S., Albani, S., and Haustein, K.:  
647 Smaller desert dust cooling effect estimated from analysis of dust size and abundance, *Nat. Geosci.*, 10, 274–  
648 278, <https://doi.org/10.1038/ngeo2912>, 2017.

649 Kok, J. F., Ward, D. S., Mahowald, N. M., and Evan, A. T.: Global and regional importance of the direct dust-climate  
650 feedback, *Nat. Commun.*, 9, 241, <https://doi.org/10.1038/s41467-017-02620-y>, 2018.

651 Kok, J. F., Adebisi, A. A., Albani, S., Balkanski, Y., Checa-Garcia, R., Chin, M., Colarco, P. R., Hamilton, D. S.,  
652 Huang, Y., Ito, A., Klose, M., Leung, D. M., Li, L., Mahowald, N. M., Miller, R. L., Obiso, V., Pérez García-  
653 Pando, C., Rocha-Lima, A., Wan, J. S., and Whicker, C. A.: Improved representation of the global dust cycle  
654 using observational constraints on dust properties and abundance, *Atmos. Chem. Phys.*, 21, 8127–8167,  
655 <https://doi.org/10.5194/acp-21-8127-2021>, 2021.

656 Lacagnina, C., Hasekamp, O. P., Bian, H., Curci, G., Myhre, G., van Noije, T., Schulz, M., Skeie, R. B., Takemura,  
657 T., and Zhang, K.: Aerosol single-scattering albedo over the global oceans: Comparing PARASOL retrievals

658 with AERONET, OMI, and AeroCom models estimates, *J. Geophys. Res.*, 120, 9814–9836,  
659 <https://doi.org/10.1002/2015JD023501>, 2015.

660 Laskin, A., Iedema, M. J., Ichkovich, A., Graber, E. R., Taraniukb, I., and Yinon, R.: Direct observation of completely  
661 processed calcium carbonate dust particles, *Faraday Discuss.*, 130, 453–468,  
662 <https://doi.org/10.1039/B417366J>, 2005.

663 Lau, K. M., Kim, K. M., Sud, Y. C., and Walker, G. K.: A GCM study of the response of the atmospheric water cycle  
664 of West Africa and the Atlantic to Saharan dust radiative forcing, *Ann. Geophys.*, 27, 4023–4037,  
665 <https://doi.org/10.5194/angeo-27-4023-2009>, 2009.

666 Li, F., Vogelmann, A. M., and Ramanathan, V.: Dust aerosol radiative forcing measured from space over the Western  
667 Africa, *J. Climate*, 17(13), 2558–2571, [https://doi.org/10.1175/1520-0442\(2004\)017<2558:SDARFM>2.0.CO;2](https://doi.org/10.1175/1520-0442(2004)017<2558:SDARFM>2.0.CO;2), 2004.

669 Li, L., and Sokolik, I. N.: The dust direct radiative impact and its sensitivity to the land surface state and key minerals  
670 in the WRF-Chem-DuMo model: A case study of dust storms in Central Asia, *J. Geophys. Res.-Atmos.*, 123,  
671 4564–4582, <https://doi.org/10.1029/2017JD027667>, 2018.

672 Liao, H. and Seinfeld, J.: Radiative forcing by mineral dust aerosols: sensitivity to key variables, *J. Geophys. Res.*,  
673 103, 31637–31645, <https://doi.org/10.1029/1998JD200036>, 1998.

674 Liu, X. H., Penner, J. E. and Herzog, M.: Global modeling of aerosol dynamics: Model description, evaluation, and  
675 interactions between sulfate and nonsulfate aerosols, *J. Geophys. Res.*, 110, D18206,  
676 doi:10.1029/2004jd005674, 2005.

677 Long, L. L., Querry, M. R., Bell, R. J., and Alexander, R. W.: Optical properties of calcite and gypsum in crystalline  
678 and powdered form in the infrared and far-infrared, *Infrared Phys.*, 34, 191–201,  
679 [https://doi.org/10.1016/0020-0891\(93\)90008-U](https://doi.org/10.1016/0020-0891(93)90008-U), 1993.

680 Lucarini, V., Saarinen, J. J., Peiponen, K.-E., and Vartiainen, E. M.: *Kramers-Kronig relations in optical materials*  
681 *research*, vol. 110, Switzerland: Springer Science & Business Media, 2005.

682 Mahowald, N., Albani, S., Kok, J. F., Engelstaeder, S., Scanza, R., Ward, D. S., and Flanner, M. G.: The size  
683 distribution of desert dust aerosols and its impact on the Earth system, *Aeolian Res.*, 15, 53–71, 2014,  
684 <https://doi.org/10.1016/j.aeolia.2013.09.002>, 2014.

685 Matsuki, A., Iwasaka, Y., Shi, G., Zhang, D., Trochkin, D., Yamada, M., Kim, Y.-S., Chen, B., Nagatani, T.,  
686 Miyazawa, T., Nagatani, M., and Nakata, H.: Morphological and chemical modification of mineral dust:  
687 Observational insight into the heterogeneous uptake of acidic gases, *Geophys. Res. Lett.*, 32, L22806,  
688 <https://doi.org/10.1029/2005gl024176>, 2005.

689 Meinshausen, M., Vogel, E., Nauels, A., Lorbacher, K., Meinshausen, N., Etheridge, D. M., Fraser, P. J., Montzka, S.  
690 A., Rayner, P. J., Trudinger, C. M., Krummel, P. B., Beyerle, U., Canadell, J. G., Daniel, J. S., Enting, I. G.,  
691 Law, R. M., Lunder, C. R., O'Doherty, S., Prinn, R. G., Reimann, S., Rubino, M., Velders, G. J. M., Vollmer,  
692 M. K., Wang, R. H. J., and Weiss, R.: Historical greenhouse gas concentrations for climate modelling  
693 (CMIP6), *Geosci. Model Dev.*, 10, 2057–2116, <https://doi.org/10.5194/gmd-10-2057-2017>, 2017.

694 Meng, Z., Yang, P., Kattawar, G. W., Bi, L., Liou, K. N., and Laszlo, I.: Single-scattering properties of tri-axial  
695 ellipsoidal mineral dust aerosols: a database for application to radiative transfer calculations, *J. Aerosol Sci.*,  
696 41, 501–512, <https://doi.org/10.1016/j.jaerosci.2010.02.008>, 2010.

697 Miller, R. L. and Tegen, I.: Climate response to soil dust aerosols, *J. Climate*, 11, 3247–3267,  
698 [https://doi.org/10.1175/1520-0442\(1998\)011<3247:CRTSDA>2.0.CO;2](https://doi.org/10.1175/1520-0442(1998)011<3247:CRTSDA>2.0.CO;2), 1998.

699 Miller, R. L., Perlwitz, J., and Tegen, I.: Feedback upon dust emission by dust radiative forcing through the planetary  
700 boundary layer, *J. Geophys. Res.*, 109, D24209, doi:10.1029/2004JD004912, 2004a.

701 Miller, R. L., Tegen, I., and Perlwitz, J.: Surface radiative forcing by soil dust aerosols and the hydrologic cycle, *J.*  
702 *Geophys. Res.*, 109, D04203, <https://doi.org/10.1029/2003JD004085>, 2004b.

703 Miller, R. L., Knippertz, P., Pérez García-Pando, C., Perlwitz, J. P., and Tegen, I.: Impact of dust radiative forcing  
704 upon climate, in: *Mineral Dust: A Key Player in the Earth System*, edited by: Knippertz, P. and Stuut, J.-B.  
705 W., Springer, 327–357, doi:10.1007/978-94-017-8978-3\_13, 2014.

706 Myriokefalitakis, S., Ito, A., Kanakidou, M., Nenes, A., Krol, M. C., Mahowald, N. M., Scanza, R. A., Hamilton, D.  
707 S., Johnson, M. S., Meskhidze, N., Kok, J. F., Guieu, C., Baker, A. R., Jickells, T. D., Sarin, M. M., Bikkina,  
708 S., Shelley, R., Bowie, A., Perron, M. M. G., and Duce, R. A.: Reviews and syntheses: the GESAMP  
709 atmospheric iron deposition model intercomparison study, *Biogeosciences*, 15, 6659–6684,  
710 <https://doi.org/10.5194/bg-15-6659-2018>, 2018.

711 Penner, J.: Soot, sulfate, dust and the climate—Three ways through the fog. *Nature*, 570, 158–159,  
712 <https://doi.org/10.1038/d41586-019-01791-6>, 2019.

713 Perlwitz, J., Tegen, I., and Miller, R.: Interactive soil dust aerosol model in the GISS GCM 1. Sensitivity of the soil  
714 dust cycle to radiative properties of soil dust aerosols, *J. Geophys. Res.*, 106(D16), 18,167–18,192,  
715 <https://doi.org/10.1029/2000JD900668>, 2001

716 Räisänen, P., Haapanala, P., Chung, C. E., Kahnert, M., Makkonen, R., Tonttila, J., and Nousiainen, T.: Impact of  
717 dust particle nonsphericity on climate simulations, *Q. J. Roy. Meteor. Soc.*, 139, 2222–2232,  
718 <https://doi.org/10.1002/qj.2084>, 2013.



719 Reichle, R. H., de Lannoy, G., Koster, R. D., Crow, W. T., Kimball, J. S., and Liu, Q.: SMAP L4 global 3-hourly 9  
720 km EASE-grid surface and root zone soil moisture geophysical data, version 4. NASA National Snow and  
721 Ice Data Center Distributed Active Archive Center, <https://doi.org/10.5067/kpjnn2gi1dqr>, 2018.

722 Reichle, R. H., Liu, Q., Koster, R. D., Crow, W. T., De Lannoy, G. J. M., Kimball, J. S., Ardizzone, J. V., Bosch, D.,  
723 Colliander, A., Cosh, M., Kolassa, J., Mahanama, S. P., Prueger, J., Starks, P., and Walker, J. P.: Version 4  
724 of the SMAP Level-4 Soil Moisture algorithm and data product. *J. Adv. Model Earth Syst.*, 11, 3106–3130,  
725 <https://doi.org/10.1029/2019MS001729>, 2019.

726 Reid, E. A., Reid, J. S., Meier, M. M., Dunlap, M. R., Cliff, S. S., Broumas, A., Perry, K., and Maring, H.:  
727 Characterization of African dust transported to Puerto Rico by individual particle and size segregated bulk  
728 analysis, *J. Geophys. Res.*, 108, 8591, <https://doi.org/10.1029/2002JD002935>, D19, 2003.

729 Ridley, D. A., Heald, C. L., Kok, J. F., and Zhao, C.: An observationally constrained estimate of global dust aerosol  
730 optical depth, *Atmos. Chem. Phys.*, 16, 15097–15117, <https://doi.org/10.5194/acp-16-15097-2016>, 2016.

731 Rosenberg, P. D., Parker, D. J., Ryder, C. L., Marsham, J. H., Garcia-Carreras, L., Dorsey, J. R., Brooks, I. M., Dean,  
732 A. R., Crosier, J., McQuaid, J. B., and Washington, R.: Quantifying particle size and turbulent scale  
733 dependence of dust flux in the Sahara using aircraft measurements, *J. Geophys. Res.-Atmos.*, 119, 7577–  
734 7598, <https://doi.org/10.1002/2013JD021255>, 2014.

735 Ryder, C. L., Highwood, E. J., Lai, T. M., Sodemann, H., and Marsham, J. H.: Impact of atmospheric transport on the  
736 evolution of microphysical and optical properties of Saharan dust, *Geophys. Res. Lett.*, 40, 2433–2438,  
737 <https://doi.org/10.1002/grl.50482>, 2013.

738 Ryder, C. L., Highwood, E. J., Walser, A., Seibert, P., Philipp, A., and Weinzierl, B.: Coarse and giant particles are  
739 ubiquitous in Saharan dust export regions and are radiatively significant over the Sahara, *Atmos. Chem.*  
740 *Phys.*, 19, 15353–15376, <https://doi.org/10.5194/acp-19-15353-2019>, 2019.

741 Sicard, M., Bertolín, S., Mallet, M., Dubuisson, P., and Comerón, A.: Estimation of mineral dust long-wave radiative  
742 forcing: sensitivity study to particle properties and application to real cases in the region of Barcelona, *Atmos.*  
743 *Chem. Phys.*, 14, 9213–9231, <https://doi.org/10.5194/acp-14-9213-2014>, 2014.

744 Sokolik, I. N., Toon, O. B., and Bergstrom, R. W.: Modeling the radiative characteristics of airborne mineral aerosols  
745 at infrared wavelengths, *J. Geophys. Res.*, 103, 8813–8826, <https://doi.org/10.1029/98JD00049>, 1998.

746 Sokolik, I. N. and Toon, O. B.: Incorporation of mineralogical composition into models of the radiative properties of  
747 mineral aerosol from UV to IR wavelengths, *J. Geophys. Res.*, 104(D8), 9423–9444,  
748 <https://doi.org/10.1029/1998JD200048>, 1999.

749 Song, Q., Zhang, Z., Yu, H., Kato, S., Yang, P., Colarco, P., Remer, L. A., and Ryder, C. L.: Net radiative effects of  
750 dust in the tropical North Atlantic based on integrated satellite observations and in situ measurements, *Atmos.*  
751 *Chem. Phys.*, 18, 11303–11322, <https://doi.org/10.5194/acp-18-11303-2018>, 2018.

752 Stegmann, P. G. and Yang, P.: A regional, size-dependent, and causal effective medium model for Asian and Saharan  
753 mineral dust refractive index spectra, *J. Aerosol Sci.*, 114, 327–341,  
754 <https://doi.org/10.1016/j.jaerosci.2017.10.003>, 2017.

755 Takemura, T., Egashira, M., Matsuzawa, K., Ichijo, H., O'ishi, R., and Abe-Ouchi, A.: A simulation of the global  
756 distribution and radiative forcing of soil dust aerosols at the Last Glacial Maximum, *Atmos. Chem. Phys.*, 9,  
757 3061–3073, <https://doi.org/10.5194/acp-9-3061-2009>, 2009.

758 Tanaka, T. Y., Aoki, T., Takahashi, H., Shibata, K., Uchiyama, A., and Mikami, M.: Study of the sensitivity of optical  
759 properties of mineral dust to the direct aerosol radiative perturbation using a global aerosol transport model,  
760 *SOLA*, 3, 33–36, <https://doi.org/10.2151/sola.2007-009>, 2007.

761 Taylor, K.E., 2001. Summarizing multiple aspects of model performance in a single diagram. *Journal of Geophysical*  
762 *Research-Atmospheres* 106, 7183-7192.

763 Tegen, I. and Lacis, A.: Modeling of particle size distribution and its influence on the radiative properties of mineral  
764 dust aerosol, *J. Geophys. Res.*, 101, 19237–19244, <https://doi.org/10.1029/95JD03610>, 1996.

765 Toth III, J. R., Rajupet, S., Squire, H., Volbers, B., Zhou, J., Xie, L., Sankaran, R. M., and Lacks, D. J.: Electrostatic  
766 forces alter particle size distributions in atmospheric dust, *Atmos. Chem. Phys.*, 20, 3181–3190,  
767 <https://doi.org/10.5194/acp-20-3181-2020>, 2020.

768 Tuccella, P., Curci, G., Pitari, G., Lee, S., and Jo, D. S.: Direct radiative effect of absorbing aerosols: sensitivity to  
769 mixing state, brown carbon and soil dust refractive index and shape, *J. Geophys. Res.-Atmos.*, 125,  
770 e2019JD030967, <https://doi.org/10.1029/2019JD030967>, 2020.

771 van der Does, M., Korte, L. F., Munday, C. I., Brummer, G.-J. A., and Stuut, J.-B. W.: Particle size traces modern  
772 Saharan dust transport and deposition across the equatorial North Atlantic, *Atmos. Chem. Phys.*, 16, 13697–  
773 13710, <https://doi.org/10.5194/acp-16-13697-2016>, 2016.

774 van der Does, M., Knippertz, P., Zschenderlein, P., Giles Harrison, R., and Stuut, J.-B. W.: The mysterious long-range  
775 transport of giant mineral dust particles, *Sci. Adv.*, 4, eaau2768, <https://doi.org/10.1126/sciadv.aau2768>,  
776 2018.

777 Volz, F.: Infrared optical constants of aerosols at some locations, *Appl. Optics*, 22, 23, 3690–3700,  
778 <https://doi.org/10.1364/AO.11.000755>, 1983.

779 Wagner, R., Ajtai, T., Kandler, K., Lieke, K., Linke, C., Müller, T., Schnaiter, M., and Vragel, M.: Complex refractive  
780 indices of Saharan dust samples at visible and near UV wavelengths: a laboratory study, *Atmos. Chem. Phys.*,  
781 12, 2491–2512, <https://doi.org/10.5194/acp-12-2491-2012>, 2012.

782 Wan, Z., Hook, S., and Hulley, G.: MOD11C2 MODIS/Terra Land Surface Temperature/Emissivity 8-Day L3 Global  
783 0.05Deg CMG V006 [Data set]. NASA EOSDIS Land Processes DAAC,  
784 <https://doi.org/10.5067/MODIS/MOD11C2.006>, 2015.

785 Wang, M. and Penner, J. E.: Aerosol indirect forcing in a global model with particle nucleation, *Atmos. Chem. Phys.*,  
786 9, 239–260, <https://doi.org/10.5194/acp-9-239-2009>, 2009.

787 Wiegner, M., Gasteiger, J., Kandler, K., Weinzierl, B., Rasp, K., Esselborn, M., Freudenthaler, V., Heese, B.,  
788 Toledano, C., Tesche, M., and Althausen, D.: Numerical simulations of optical properties of Saharan dust  
789 aerosols with emphasis on lidar applications, *Tellus B*, 61, 180–194, <https://doi.org/10.1111/j.1600-0889.2008.00381.x>, 2009.

791 Xu, L. and Penner, J. E.: Global simulations of nitrate and ammonium aerosols and their radiative effects, *Atmos.*  
792 *Chem. Phys.*, 12, 9479–9504, <https://doi.org/10.5194/acp-12-9479-2012>, 2012.

793 Yang, E.-S., Gupta, P., and Christopher, S. A.: Net radiative effect of dust aerosols from satellite measurements over  
794 Sahara, *Geophys. Res. Lett.*, 36, L18812, <https://doi.org/10.1029/2009GL039801>, 2009.

795 Yoshioka, M., Mahowald, N., Conley, A. J., Collins, W. D., Fillmore, D.W., Zender, C. S., and Coleman, D. B.:  
796 Impact of desert dust radiative forcing on Sahel precipitation: relative importance of dust compared to sea  
797 surface temperature variations, vegetation changes and greenhouse gas warming, *J. Climate*, 16, 1445–1467,  
798 <https://doi.org/10.1175/JCLI4056.1>, 2007.

799 Zhang, D., and Iwasaka, Y.: Size change of Asian dust particles caused by sea salt interaction: Measurements in  
800 southwestern Japan, *Geophys. Res. Lett.*, 31, L15102, <https://doi.org/10.1029/2004GL020087>, 2004.

801 Zhang, J. and Christopher, S. A.: Longwave radiative forcing of Saharan dust aerosols estimated from MODIS, MISR,  
802 and CERES observations on Terra, *Geophys. Res., Lett.*, 30(23), 2188,  
803 <https://doi.org/10.1029/2003GL018479>, 2003.

804 Zhao, C., Chen, S., Leung, L. R., Qian, Y., Kok, J. F., Zaveri, R. A., and Huang, J.: Uncertainty in modeling dust mass  
805 balance and radiative forcing from size parameterization, *Atmos. Chem. Phys.*, 13, 10733–10753,  
806 <https://doi.org/10.5194/acp-13-10733-2013>, 2013.

807 Zhou, Y., Levy, R. C., Remer, L. A., Mattoo, S., and Espinosa, W. R.: Dust aerosol retrieval over the oceans with the  
808 MODIS/VIIRS dark target algorithm: 2. Nonspherical dust model, *Earth Space Sci.*, 7, e2020EA001222,  
809 <https://doi.org/10.1029/2020EA001222>, 2020.

810 **Figure captions**

811 Figure 1. Imaginary part of the refractive index at (a) 0.52  $\mu\text{m}$ , (b) SW, (c) 9.7  $\mu\text{m}$ , and (d) LW. The refractive  
812 index obtained from 19 samples was aggregated into 9 main source regions and the arithmetic mean was  
813 calculated for each source region (Di Biagio et al., 2017, 2019). The global mean is used for others. The  
814 coordinates of the nine source regions were: (S1) western North Africa (20°W – 7.5°E; 18°N – 37.5°N), (S2)  
815 eastern North Africa (7.5°E – 35°E; 18°N – 37.5°N), (S3) the Sahel (20°W – 35°E; 0°N – 18°N), (S4) Middle  
816 East / Central Asia (30°E – 70°E for 0°N – 35°N, and 30°E – 75°E for 35°N – 50°N), (S5) East Asia (70°E  
817 – 120°E; 35°N – 50°N), (S6) North America (130°W – 80°W; 20°N – 45°N), (S7) Australia (110°E – 160°E;  
818 10°S – 40°S), (S8) South America (80°W – 20°W; 0°S – 60°S), and (S9) Southern Africa (0°E – 40°E; 0°S  
819 – 40°S).

820 Figure 2. The model better reproduced semi-observationally-based data of DAOD<sub>550</sub> after adjusting the size-  
821 resolved dust load with DustCOMM and considering the dust asphericity. (a) semi-observationally-based  
822 estimates of the DAOD<sub>550</sub> were averaged over 2004–2008 (Ridley et al., 2016; Adebisi et al., 2020). The  
823 annually averaged model results were shown for (b) DustCOMM-Asphere-DB19-V83 (E2) and (c) the  
824 differences between IMPACT-Sphere-Mineral-V83 (E1) and E2 simulations. (d) Comparison of seasonally  
825 averaged DAOD<sub>550</sub> for semi-observationally-based (SOB) data, E1, E2, IMPACT-Asphere-DB19-DB17  
826 (E3), and DustCOMM-Sphere-DB19-DB17 (E5). The square symbol represents the mean. The solid line  
827 within the box mark shows the median. The boundaries of the box mark the 25th and 75th percentiles. The  
828 whiskers above and below the box indicate the 1.5  $\times$  interquartile range, and the points indicate the outside  
829 of the range. (e) Taylor diagram summarizing the statistics of the comparison against the seasonally averaged  
830 regional DAOD<sub>550</sub> for the different experiments. The horizontal axis shows the standard deviation of the data  
831 set or model prediction, the curved axis shows the correlation, and the green dashed lines denote the root-  
832 mean-squared errors between the semi-observationally-based data and the model predictions. As such, the  
833 distance between the semi-observationally-based data and the model predictions is a measure of the model's  
834 ability to reproduce the spatiotemporal variability in the semi-observationally-based data. The coordinates  
835 and the values of DAOD<sub>550</sub> at the 15 regions (marked in Fig. 3a) in summer were listed in Table S1. The  
836 comparison for other seasons was presented in Table S2.

837 Figure 3. Model-simulated dust loads at fine (smaller than 2.5  $\mu\text{m}$  of diameter) and coarse size ranges (larger  
838 than 2.5  $\mu\text{m}$  of diameter) before and after adjusting the size-resolved dust load with DustCOMM. Results  
839 were shown for (a) fine dust from DustCOMM, (b) fine dust from IMPACT-Sphere-Mineral-V83 (E1), (c)  
840 fine dust from DustCOMM-Asphere-DB19-V83 (E2), (d) coarse dust from DustCOMM, (e) coarse dust from

841 E1, and (f) coarse dust from E2 simulations. The parentheses represented the global dust burden ( $T_g$ ). The  
842 values of dust load at each bin were listed in Table 3.

843 Figure 4. Dust clear-sky SW radiative effect efficiency ( $W \cdot m^{-2} DAOD^{-1}$ ). Semi-observationally-based data  
844 at (a) the surface and (b) TOA were based on satellite observations (Yang et al. 2009; Li et al., 2004; Song  
845 et al., 2018; Christopher and Jones, 2007). The model results were shown for (c) and (d) IMPACT-Sphere-  
846 Mineral-V83 (E1), and (e) and (f) DustCOMM-Asphere-DB19-V83 (E2) simulations at the surface and TOA,  
847 respectively. Comparison of seasonally averaged SW radiative effect efficiency for semi-observationally-  
848 based (SOB) data and the different experiments at (g) the surface and (h) TOA. The square symbol represents  
849 the mean. The solid line within the box mark shows the median. The boundaries of the box mark the 25th  
850 and 75th percentiles. The whiskers above and below the box indicate the  $1.5 \times$  interquartile range, and the  
851 points indicate the outside of the range. Taylor diagram summarizing the statistics of the comparison against  
852 the seasonally averaged regional SW radiative effect efficiency for the different experiments at (i) the surface  
853 and (j) TOA. The horizontal axis shows the standard deviation of the data set or model prediction, the curved  
854 axis shows the correlation, and the green dashed lines denote the root-mean-squared errors between the semi-  
855 observationally-based data and the model predictions. As such, the distance between the semi-  
856 observationally-based data and the model predictions is a measure of the model's ability to reproduce the  
857 spatiotemporal variability in the semi-observationally-based data. The regionally averaged values were listed  
858 in Tables S3 and S4 at the surface and TOA, respectively.

859 Figure 5. Dust clear-sky LW radiative effect efficiency ( $W \cdot m^{-2} DAOD^{-1}$ ). Semi-observationally-based  
860 estimates at (a) surface and (b) TOA were based on satellite observations (Song et al., 2018; Christopher and  
861 Jones, 2007; Zhang and Christopher, 2003; Brindley and Russell, 2009; Yang et al., 2009). The model results  
862 were shown for (c) and (d) IMPACT-Sphere-Mineral-V83 (E1), and (e) and (f) DustCOMM-Asphere-DB19-  
863 V83 (E2) simulations at the surface and TOA, respectively. Comparison of seasonally averaged LW radiative  
864 effect efficiency for semi-observationally-based (SOB) data and the different experiments at (g) the surface  
865 and (h) TOA. The square symbol represents the mean. The solid line within the box mark shows the median.  
866 The boundaries of the box mark the 25th and 75th percentiles. The whiskers above and below the box indicate  
867 the  $1.5 \times$  interquartile range, and the points indicate the outside of the range. Taylor diagram summarizing  
868 the statistics of the comparison against the seasonally averaged regional SW radiative effect efficiency for  
869 the different experiments at (i) the surface and (j) TOA. The horizontal axis shows the standard deviation of  
870 the data set or model prediction, the curved axis shows the correlation, and the green dashed lines denote the  
871 root-mean-squared errors between the semi-observationally-based data and the model predictions. As such,

872 the distance between the semi-observationally-based data and the model predictions is a measure of the  
873 model's ability to reproduce the spatiotemporal variability in the semi-observationally-based data. The  
874 regionally averaged values were listed in Tables S5 and S6 at the surface and TOA, respectively.

875 Figure 6. Dust SW radiative effect ( $W \cdot m^{-2}$ ) and radiative heating of the atmosphere (i.e., the subtraction of  
876 radiative effects from TOA to the surface in unit of  $W \cdot m^{-2}$ ). The model results were shown for the simulations  
877 for (a) IMPACT-Sphere-Mineral-V83 (E1) at the surface, (b) DustCOMM-Asphere-DB19-V83 (E2) at the  
878 surface, (c) E1 in atmospheric column, (d) E2 in atmospheric column, (e) E1 at TOA, and (f) E2 simulations  
879 at TOA. The numbers in parentheses represented the global mean.

880 Figure 7. Dust LW radiative effect ( $W \cdot m^{-2}$ ) and radiative heating of the atmosphere (i.e., the subtraction of  
881 radiative effects from TOA to the surface in unit of  $W \cdot m^{-2}$ ). The model results were shown for the simulations  
882 for (a) IMPACT-Sphere-Mineral-V83 (E1) at the surface, (b) DustCOMM-Asphere-DB19-V83 (E2) at the  
883 surface, (c) E1 in atmospheric column, (d) E2 in atmospheric column, (e) E1 at TOA, and (f) E2 simulations  
884 at TOA. The numbers in parentheses represented the global mean.

885 Figure 8. Dust net radiative effect ( $W \cdot m^{-2}$ ) and radiative heating of the atmosphere (i.e., the subtraction of  
886 radiative effects from TOA to the surface in unit of  $W \cdot m^{-2}$ ). The model results were shown for the simulations  
887 for (a) IMPACT-Sphere-Mineral-V83 (E1) at the surface, (b) DustCOMM-Asphere-DB19-V83 (E2) at the  
888 surface, (c) E1 in atmospheric column, (d) E2 in atmospheric column, (e) E1 at TOA, and (f) E2 simulations  
889 at TOA. The numbers in parentheses represented the global mean.

890 Figure 9. Variability of dust radiative effect ( $W \cdot m^{-2}$ ) in different model simulations at the surface and TOA  
891 for (a) total dust SW, (b) total dust LW, and (c) total dust NET. The annually averaged values were listed in  
892 Table 5.

893 Figure 10. Radiative effect ( $W \cdot m^{-2}$ ) of mineral dust due to various aerosol absorptivity at the surface and TOA  
894 for (a) total dust SW, (b) total dust LW, and (c) total dust NET. The annually averaged values were listed in  
895 Table 5. The dashed line represented a 1 : 1 correspondence and corresponded to no change in radiative  
896 heating within the atmosphere.

**Table 1.** Summary of ten combinations of different numerical experiments compared in this study.

Number	Experiment	Size-resolved dust	Sphericity	SW refractive index	LW refractive index
E1	IMPACT-Sphere-Mineral-V83	IMPACT	Sphere	Mineralogical map <sup>d</sup>	Volz (1983)
E2 <sup>a</sup>	DustCOMM-Asphere-DB19-V83	DustCOMM <sup>b</sup>	Asphere <sup>c</sup>	Di Biagio et al. (2019)	Volz (1983)
E3	IMPACT-Asphere-DB19-DB17	IMPACT	Asphere <sup>c</sup>	Di Biagio et al. (2019)	Di Biagio et al. (2017)
E4	DustCOMM-Asphere-DB19-DB17	DustCOMM <sup>b</sup>	Asphere <sup>c</sup>	Di Biagio et al. (2019)	Di Biagio et al. (2017)
E5	DustCOMM-Sphere-DB19-DB17	DustCOMM <sup>b</sup>	Sphere	Di Biagio et al. (2019)	Di Biagio et al. (2017)
E6	DustCOMM-Asphere-Mineral-V83	DustCOMM <sup>b</sup>	Asphere <sup>c</sup>	Mineralogical map <sup>d</sup>	Volz (1983)
E7	DustCOMM-Asphere-Less-More	DustCOMM <sup>b</sup>	Asphere <sup>c</sup>	Less SW <sup>e</sup>	More LW <sup>g</sup>
E8	DustCOMM-Asphere-Less-Less	DustCOMM <sup>b</sup>	Asphere <sup>c</sup>	Less SW <sup>e</sup>	Less LW <sup>h</sup>
E9	DustCOMM-Asphere-More-More	DustCOMM <sup>b</sup>	Asphere <sup>c</sup>	More SW <sup>f</sup>	More LW <sup>g</sup>
E10	DustCOMM-Asphere-More-Less	DustCOMM <sup>b</sup>	Asphere <sup>c</sup>	More SW <sup>f</sup>	Less LW <sup>h</sup>

<sup>a</sup>Combination of DustCOMM-Asphere-DB19-DB17 (E4) for SW and DustCOMM-Asphere-Mineral-V83 (E6) for LW.

<sup>b</sup>Size-resolved dust concentration was adjusted with semi-observationally-based estimate (Adebiyi & Kok, 2020).

<sup>c</sup>Dust asphericity was considered in calculating the optical properties, which further assumed internal mixing of minerals (Huang et al., 2021) using a volume-weighted mixture for each size bin.

<sup>d</sup>Mineralogical composition of dust aerosol for each size was prescribed at emission by mineralogical map (Journet et al., 2014; Ito and Shi 2016). The more absorptive SW refractive indices (Bedidi and Cervelle, 1993; Stegmann & Yang, 2017; Long et al., 1993) were used for mineral dust, compared to the less absorptive global mean data set (Di Biagio et al., 2019).

<sup>e</sup>Less absorptive SW refractive indices were calculated by varying the values of the imaginary parts of the refractive index within the range of values from Di Biagio et al. (2019) (10% percentile).

<sup>f</sup>More absorptive SW refractive indices were calculated by varying the values of the imaginary parts of the refractive index within the range of values from Di Biagio et al. (2019) (90% percentile).

<sup>g</sup>More absorptive LW refractive indices were calculated by varying the values of the imaginary parts of the refractive index within the range of values from Di Biagio et al. (2017) (90% percentile).

<sup>h</sup>Less absorptive LW refractive indices were calculated by varying the values of the imaginary parts of the refractive index within the range of values from Di Biagio et al. (2017) (10% percentile).

**Table 2.** Summary of radiative effects estimated in this study.

SW radiative effect	LW radiative effect	Difference
Less absorptive SW, coarser particle size, & aspherical shape	Coarser particle size & aspherical shape	E2 – E1
Less absorptive SW & aspherical shape	Less absorptive LW & aspherical shape	E3 – E1
Size-resolved dust abundance	Size-resolved dust abundance	E3 – E4
Aspherical shape	Aspherical shape	E5 – E4
Mineralogical variability in refractive index (more absorptive SW)	Mineralogical variability in refractive index (more absorptive LW)	E6 – E4
Less absorptive SW (10% percentile)	More absorptive LW (90% percentile)	E7 – E4
Less absorptive SW (10% percentile)	Less absorptive LW (10% percentile)	E8 – E4
More absorptive SW (90% percentile)	More absorptive LW (90% percentile)	E9 – E4
More absorptive SW (90% percentile)	Less absorptive LW (10% percentile)	E10 – E4



**Table 3.** Annually averages of dust load (Tg), mass extinction efficiency ( $\text{m}^2 \cdot \text{g}^{-1}$ ), and  $\text{DAOD}_{550}$  at each bin on a global scale. The size-resolved dust concentration and shape in IMPACT-Sphere-Mineral-V83 (E1) simulation was adjusted to DustCOMM in DustCOMM-Asphere-DB19-V83 (E2) simulation. At the same time, we maintained the consideration of asphericity on the gravitational velocity and kept the dust concentrations unaltered between IMPACT-Sphere-Mineral-V83 (E1) and IMPACT-Asphere-DB19-DB17 simulations (E3).

Dust size bin	Dust load			Mass extinction efficiency				$\text{DAOD}_{550}$			
	E1	E2	DustCOMM	E1	E2	E3	DustCOMM	E1	E2	E3	DustCOMM
Bin 1 <sup>a</sup>	1.2	0.8	$1.2 \pm 0.7$	2.11	3.41	3.33	3.06	0.0050	0.0055	0.0078	0.0070
Bin 2 (1.26–2.5 $\mu\text{m}$ )	4.7	2.6	$3.5 \pm 2.1$	0.73	1.25	1.21	1.22	0.0067	0.0064	0.0111	0.0084
Bin 3 (2.5–5 $\mu\text{m}$ )	8.2	6.2	$6.8 \pm 3.8$	0.37	0.59	0.57	0.57	0.0060	0.0071	0.0092	0.0077
Bin 4 (5–20 $\mu\text{m}$ )	10.9	22.2	$16.8 \pm 9.0$	0.23	0.24	0.29	0.19	0.0050	0.0104	0.0063	0.0063
Sum of 4 bins	25.0	31.8	$28.4 \pm 15.5$	0.46	0.47	0.70	0.53	0.0227	0.0295	0.0345	0.0294

<sup>a</sup>Bin 1 in IMPACT-Sphere-Mineral-V83 (E1) is 0.1–1.26  $\mu\text{m}$ , whereas bin1 in DustCOMM-Asphere-DB19-V83 (E2) and DustCOMM is 0.2–1.26  $\mu\text{m}$ .

**Table 4.** Semi-observationally-based data set of clear-sky dust radiative effect efficiency at the surface and TOA.

Number	Region name	Season	Region coordinates	Aerosol type selection	AOD data
R1 <sup>a</sup>	Sahara Desert	Summer	15°–30°N, 10°W–30°E	No selection	OMI-MISR
R2 <sup>b</sup>	Tropical Atlantic	Summer	15°–25°N, 45°–15°W	MODIS effective radius peaks 0.8–0.9 $\mu\text{m}$	MODIS
R3 <sup>c</sup>	Tropical Atlantic	Summer	10°–30°N, 45°–20°W	CALIOP dust and polluted dust	CERES-CALIPSO-CloudSat-MODIS
R4 <sup>d</sup>	Atlantic Ocean	Summer	0°–30°N, 60°–10°W	Dust detection based on DAOD <sub>550</sub> and fraction	MODIS
R5 <sup>e,f</sup>	North Africa	Summer	15°–35°N, 18°W–40°E	No selection	MISR <sup>e</sup> or SEVIRI <sup>f</sup>
R6 <sup>e,f</sup>	West Africa	Summer	16°–28°N, 16°–4°W	No selection	MISR <sup>e</sup> or SEVIRI <sup>f</sup>
R7 <sup>e,f</sup>	Niger-Chad	Summer	15°–20°N, 15°–22°E	No selection	MISR <sup>e</sup> or SEVIRI <sup>f</sup>
R8 <sup>e,f</sup>	Sudan	Summer	15°–22°N, 22°–36°E	No selection	MISR <sup>e</sup> or SEVIRI <sup>f</sup>
R9 <sup>e,f</sup>	Egypt-Israel	Summer	23°–32°N, 23°–35°E	No selection	MISR <sup>e</sup> or SEVIRI <sup>f</sup>
R10 <sup>e,f</sup>	North Libya	Summer	27°–33°N, 15°–25°E	No selection	MISR <sup>e</sup> or SEVIRI <sup>f</sup>
R11 <sup>e,f</sup>	South Libya	Summer	23°–27°N, 15°–25°E	No selection	MISR <sup>e</sup> or SEVIRI <sup>f</sup>
R12 <sup>g</sup>	Mediterranean	Summer	35.5°N, 12.6°E	Dust detection based on optical property	Ground-based measurements
R13 <sup>h</sup>	Cape Verde	Summer	16.7°N, 22.9°E	Dust detection based on brightness temperature	Ground-based measurements
R14 <sup>i</sup>	China	Spring	39°N, 101°E	Dust detection based on brightness temperature	Ground-based measurements

<sup>a</sup>Yang et al. (2009). <sup>b</sup>Li et al. (2004). <sup>c</sup>Song et al. (2018). <sup>d</sup>Christopher and Jones (2007). <sup>e</sup>Zhang and Christopher (2003). <sup>f</sup>Brindley and Russell (2009). <sup>g</sup>Di Biagio et al. (2010). <sup>h</sup>Hansell et al. (2010). <sup>i</sup>Hansell et al. (2012).

**Table 5.** Annually averages of short-wave (SW) ( $W \cdot m^{-2}$ ), long-wave (LW) ( $W \cdot m^{-2}$ ), and net radiative effect (NET) ( $W \cdot m^{-2}$ ) at the surface, TOA, and atmospheric radiative heating on a global scale.

Number	Data	Total dust SW		Total dust LW		Total dust NET	
		TOA (surface) <sup>a</sup>	Atmosphere	TOA (surface) <sup>a</sup>	Atmosphere	TOA (surface) <sup>a</sup>	Atmosphere
E1	IMPACT-Sphere-Mineral-V83	-0.18 (-1.26)	1.07	+0.18 (0.66)	-0.48	-0.00 (-0.60)	0.59
E2	DustCOMM-Asphere-DB19-V83	<b>-0.32 (-1.23)<sup>b</sup></b>	<b>0.91<sup>b</sup></b>	<b>+0.23 (1.00)<sup>b</sup></b>	<b>-0.77<sup>b</sup></b>	<b>-0.08 (-0.23)<sup>b</sup></b>	<b>0.15<sup>b</sup></b>
E3	IMPACT-Asphere-DB19-DB17	-0.49 (-1.35)	0.86	+0.12 (0.50)	-0.38	-0.37 (-0.84)	0.48
E4	DustCOMM-Asphere-DB19-DB17	<b>-0.32 (-1.23)<sup>b</sup></b>	<b>0.91<sup>b</sup></b>	+0.12 (0.58)	-0.46	-0.20 (-0.65)	0.45
E5	DustCOMM-Sphere-DB19-DV17	-0.28 (-0.90)	0.62	+0.08 (0.43)	-0.34	-0.20 (-0.47)	0.28
E6	DustCOMM-Asphere-Mineral-V83	+0.02 (-1.61)	1.63	<b>+0.23 (1.00)<sup>b</sup></b>	<b>-0.77<sup>b</sup></b>	+0.25 (-0.62)	0.87
E7	DustCOMM-Asphere-Less-More	-0.54 (-0.98)	0.43	+0.16 (0.76)	-0.60	-0.38 (-0.22)	-0.16
E8	DustCOMM-Asphere-Less-Less	-0.54 (-0.98)	0.43	+0.06 (0.35)	-0.29	-0.48 (-0.36)	0.15
E9	DustCOMM-Asphere-More-More	-0.08 (-1.51)	1.43	+0.16 (0.76)	-0.60	+0.09 (-0.75)	0.84
E10	DustCOMM-Asphere-More-Less	-0.08 (-1.51)	1.43	+0.06 (0.35)	-0.29	-0.01 (-1.16)	1.15
	DustCOMM (Adebisi & Kok, 2020)	-0.59 to 0.17 <sup>c</sup>		+0.25 to 0.41 <sup>c</sup>		-0.27 to 0.14 <sup>c</sup>	
M1	Miller et al. (2004b)	-0.33 (-1.82)	1.49	+0.15 (0.18)	-0.03	-0.18 (-1.64)	1.46
M2	Tanaka et al. (2007)	-0.38 (-1.22)	0.84	+0.16 (0.57)	-0.41	-0.22 (-0.65)	0.43
M3	Yoshioka et al. (2007)	-0.92 (-1.59)	0.67	+0.31 (1.13)	-0.81	-0.60 (-0.46)	-0.14
M4	Takemura et al. (2009)	-0.10 (-0.38)	0.28	+0.09 (0.18)	-0.09	-0.01 (-0.20)	0.19
M5	Albani et al. (2014)	-0.38 (-1.20)	0.81	+0.15 (0.64)	-0.49	-0.23 (-0.56)	0.33
M6	Colarco et al. (2014)	-0.32 (-1.25)	0.93	+0.05 (0.30)	-0.25	-0.27 (-0.95)	0.68
M7	Di Biagio et al. (2020)	-0.29 (-1.17) <sup>d</sup>	0.88 <sup>d</sup>	+0.23 (0.48) <sup>d</sup>	-0.26 <sup>d</sup>	-0.06 (-0.69) <sup>d</sup>	0.63 <sup>d</sup>
M8	Balkanski et al. (2021)	-0.14 (-1.42)	1.28	+0.12 (0.41)	-0.29	-0.02 (-1.01)	0.98

<sup>a</sup>The parentheses represent the RE at the surface. <sup>b</sup>The bold represents the combination of DB19 for SW and V83 for LW (i.e., DustCOMM-Asphere-DB19-V83). <sup>c</sup>98% confidential interval of DustCOMM data set is listed. <sup>d</sup>For a comparison with our estimates, sum of single mode simulations from Di Biagio et al. (2019) is listed.

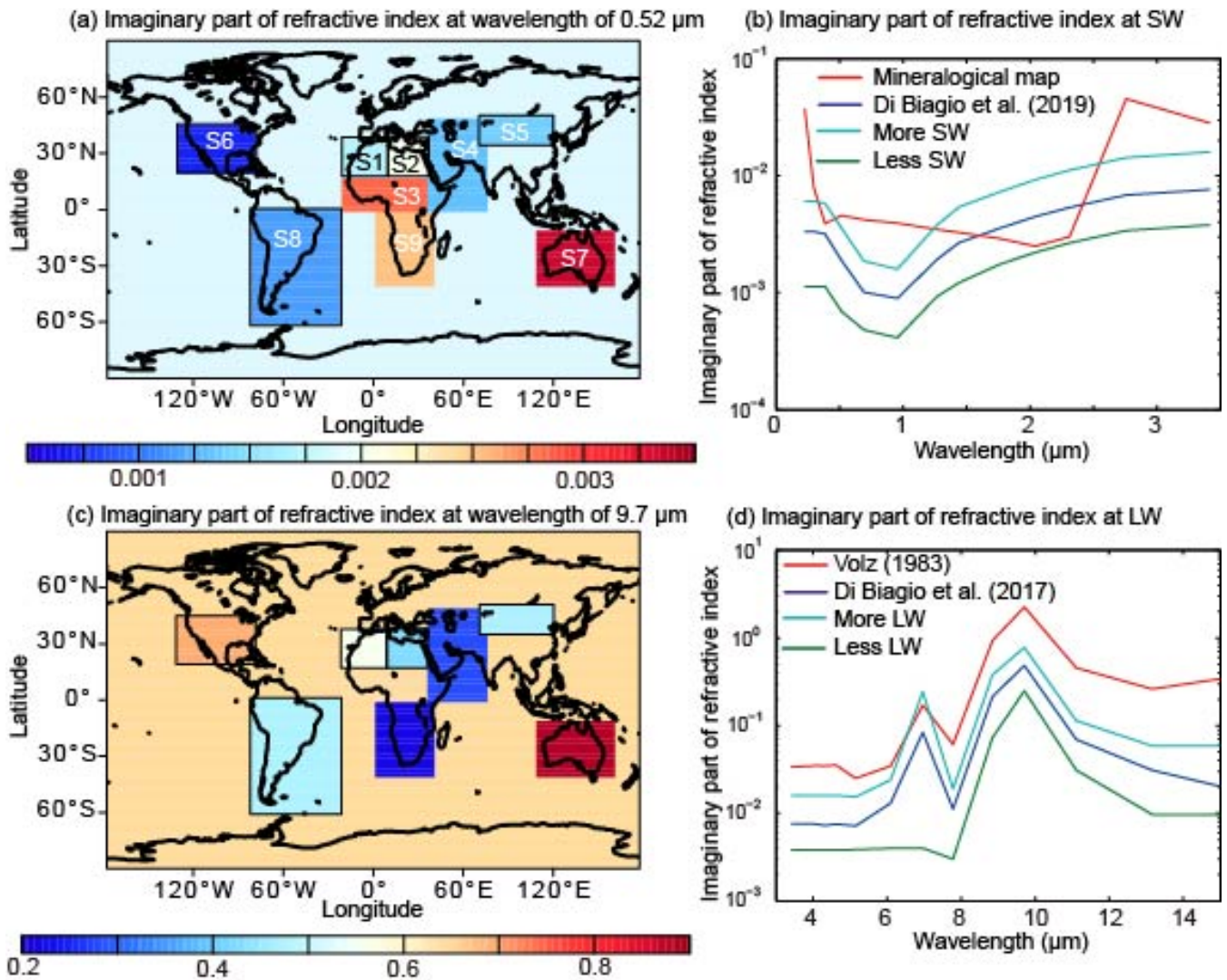


**Figure 1.** Imaginary part of the refractive index at (a) 0.52  $\mu\text{m}$ , (b) SW, (c) 9.7  $\mu\text{m}$ , and (d) LW. The refractive index obtained from 19 samples was aggregated into 9 main source regions and the arithmetic mean was calculated for each source region (Di Biagio et al., 2017, 2019). The global mean is used for others. The coordinates of the nine source regions were: (S1) western North Africa (20°W – 7.5°E; 18°N – 37.5°N), (S2) eastern North Africa (7.5°E – 35°E; 18°N – 37.5°N), (S3) the Sahel (20°W – 35°E; 0°N – 18°N), (S4) Middle East / Central Asia (30°E – 70°E for 0°N – 35°N, and 30°E – 75°E for 35°N – 50°N), (S5) East Asia (70°E – 120°E; 35°N – 50°N), (S6) North America (130°W – 80°W; 20°N – 45°N), (S7) Australia (110°E – 160°E; 10°S – 40°S), (S8) South America (80°W – 20°W; 0°S – 60°S), and (S9) Southern Africa (0°E – 40°E; 0°S – 40°S).

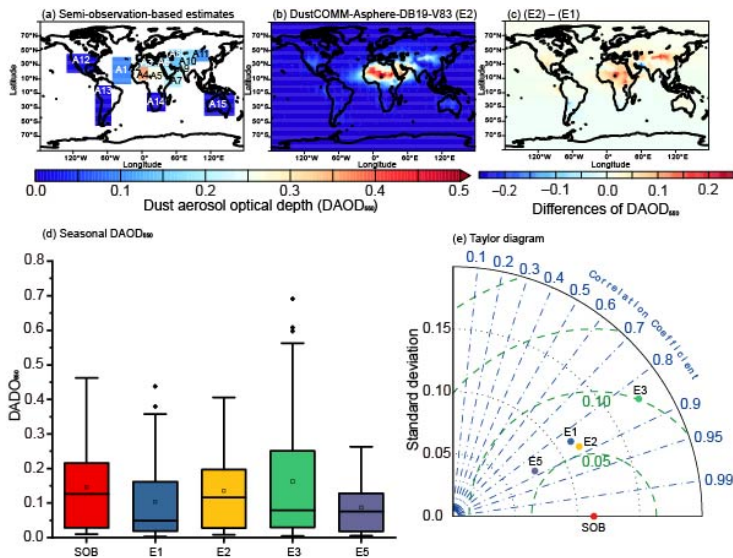


**Figure 2.** The model better reproduced semi-observationally-based data of DAOD<sub>550</sub> after adjusting the size-resolved dust load with DustCOMM and considering the dust asphericity. (a) semi-observationally-based estimates of the DAOD<sub>550</sub> were averaged over 2004–2008 (Ridley et al., 2016; Adebisi et al., 2020). The annually averaged model results were shown for (b) DustCOMM-Asphere-DB19-V83 (E2) and (c) the differences between IMPACT-Sphere-Mineral-V83 (E1) and E2 simulations. (d) Comparison of seasonally averaged DAOD<sub>550</sub> for semi-observationally-based (SOB) data, E1, E2, IMPACT-Asphere-DB19-DB17 (E3), and DustCOMM-Sphere-DB19-DB17 (E5). The square symbol represents the mean. The solid line within the box mark shows the median. The boundaries of the box mark the 25th and 75th percentiles. The whiskers above and below the box indicate the  $1.5 \times$  interquartile range, and the points indicate the outside of the range. (e) Taylor diagram summarizing the statistics of the comparison against the seasonally averaged regional DAOD<sub>550</sub> for the different experiments. The horizontal axis shows the standard deviation of the data set or model prediction, the curved axis shows the correlation, and the green dashed lines denote the root-mean-squared errors between the semi-observationally-based data and the model predictions. As such, the distance between the semi-observationally-based data and the model predictions is a measure of the model’s ability to reproduce the spatiotemporal variability in the semi-observationally-based data. The coordinates and the values of DAOD<sub>550</sub> at the 15 regions (marked in Fig. 2a) in summer were listed in Table S1. The comparison for other seasons was presented in Table S2.

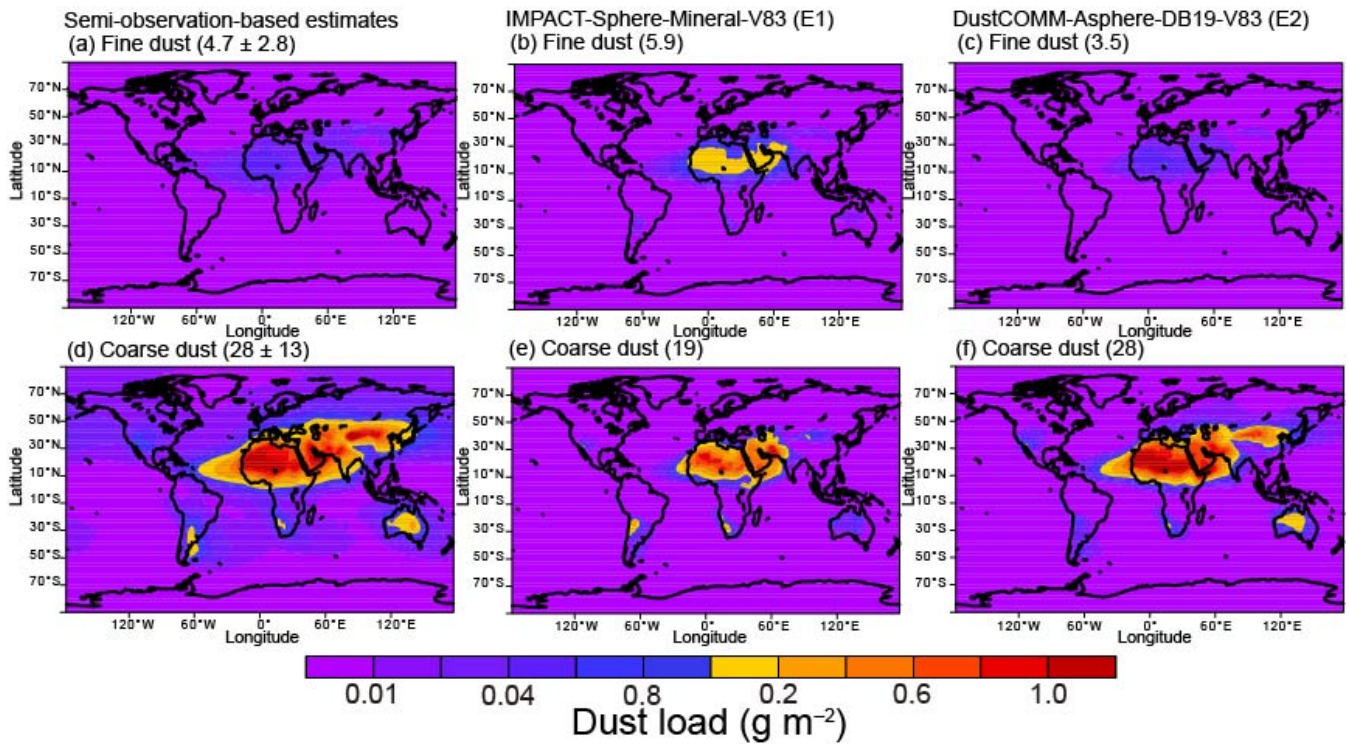


**Figure 3.** Model-simulated dust loads at fine (smaller than 2.5  $\mu\text{m}$  of diameter) and coarse size ranges (larger than 2.5  $\mu\text{m}$  of diameter) before and after adjusting the size-resolved dust load with DustCOMM. Results were shown for (a) fine dust from DustCOMM, (b) fine dust from IMPACT-Sphere-Mineral-V83 (E1), (c) fine dust from DustCOMM-Asphere-DB19-V83 (E2), (d) coarse dust from DustCOMM, (e) coarse dust from E1, and (f) coarse dust from E2 simulations. The parentheses represented the global dust burden ( $T_g$ ). The values of dust load at each bin were listed in Table 3.

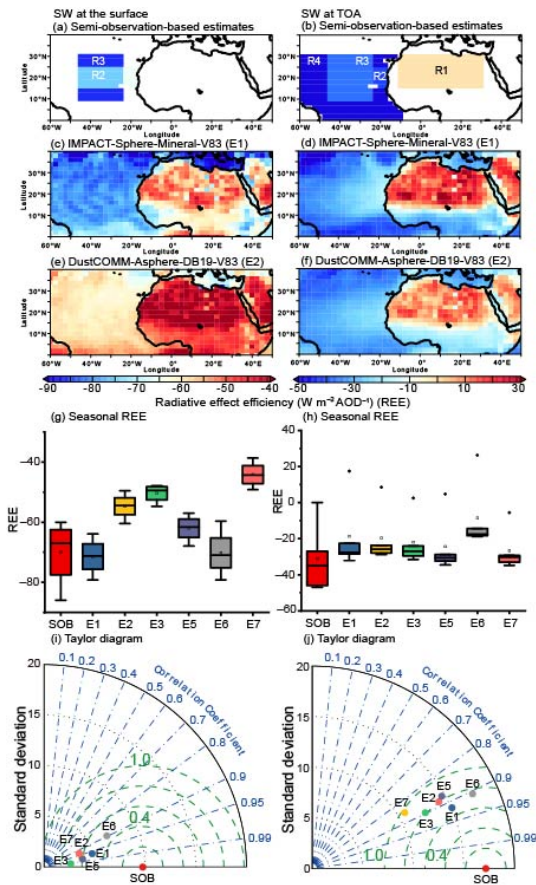


**Figure 4.** Dust clear-sky SW radiative effect efficiency ( $W \cdot m^{-2} DAOD^{-1}$ ). Semi-observationally-based data at (a) the surface and (b) TOA were based on satellite observations (Yang et al. 2009; Li et al., 2004; Song et al., 2018; Christopher and Jones, 2007). The model results were shown for (c) and (d) IMPACT-Sphere-Mineral-V83 (E1), and (e) and (f) DustCOMM-Asphere-DB19-V83 (E2) simulations at the surface and TOA, respectively. Comparison of seasonally averaged SW radiative effect efficiency for semi-observationally-based (SOB) data and the different experiments at (g) the surface and (h) TOA. The square symbol represents the mean. The solid line within the box mark shows the median. The boundaries of the box mark the 25th and 75th percentiles. The whiskers above and below the box indicate the  $1.5 \times$  interquartile range, and the points indicate the outside of the range. Taylor diagram summarizing the statistics of the comparison against the seasonally averaged regional SW radiative effect efficiency for the different experiments at (i) the surface and (j) TOA. The horizontal axis shows the standard deviation of the data set or model prediction, the curved axis shows the correlation, and the green dashed lines denote the root-mean-squared errors between the semi-observationally-based data and the model predictions. As such, the distance between the semi-observationally-based data and the model predictions is a measure of the model's ability to reproduce the spatiotemporal variability in the semi-observationally-based data. The regionally averaged values were listed in Tables S3 and S4 at the surface and TOA, respectively.



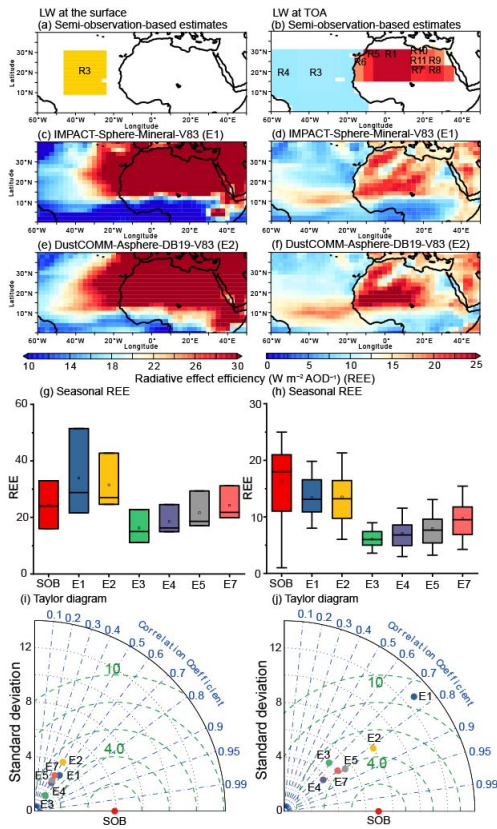
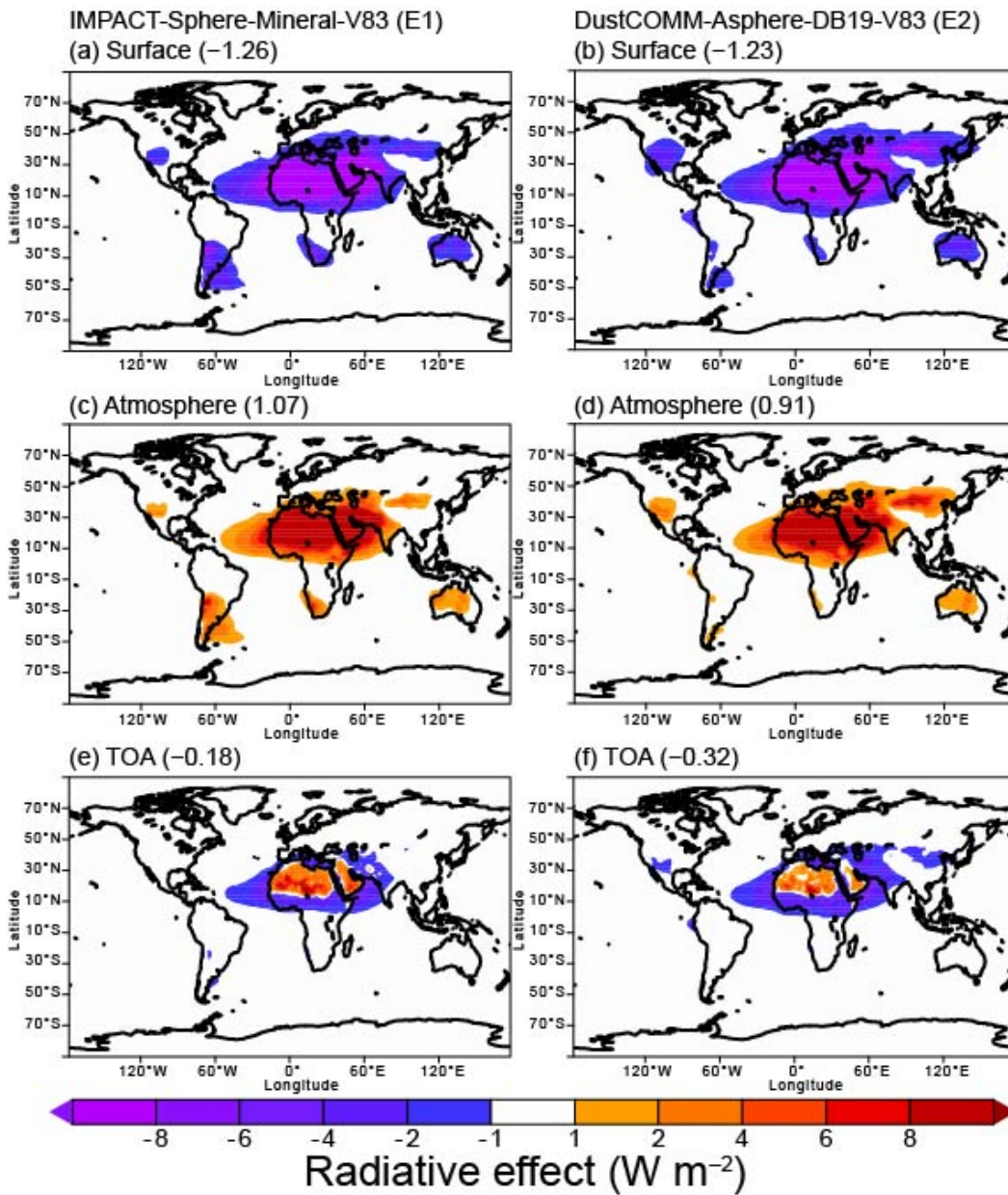


**Figure 5.** Dust clear-sky LW radiative effect efficiency ( $W \cdot m^{-2} \cdot DAOD^{-1}$ ). Semi-observationally-based estimates at (a) surface and (b) TOA were based on satellite observations (Song et al., 2018; Christopher and Jones, 2007; Zhang and Christopher, 2003; Brindley and Russell, 2009; Yang et al., 2009). The model results were shown for (c) and (d) IMPACT-Sphere-Mineral-V83 (E1), and (e) and (f) DustCOMM-Asphere-DB19-V83 (E2) simulations at the surface and TOA, respectively. Comparison of seasonally averaged LW radiative effect efficiency for semi-observationally-based (SOB) data and the different experiments at (g) the surface and (h) TOA. The square symbol represents the mean. The solid line within the box mark shows the median. The boundaries of the box mark the 25th and 75th percentiles. The whiskers above and below the box indicate the  $1.5 \times$  interquartile range, and the points indicate the outside of the range. Taylor diagram summarizing the statistics of the comparison against the seasonally averaged regional SW radiative effect efficiency for the different experiments at (i) the surface and (j) TOA. The horizontal axis shows the standard deviation of the data set or model prediction, the curved axis shows the correlation, and the green dashed lines denote the root-mean-squared errors between the semi-observationally-based data and the model predictions. As such, the distance between the semi-observationally-based data and the model predictions is a measure of the model's ability to reproduce the spatiotemporal variability in the semi-observationally-based data. The regionally averaged values were listed in Tables S5 and S6 at the surface and TOA, respectively.



65

**Figure 6.** Dust SW radiative effect ( $\text{W} \cdot \text{m}^{-2}$ ) and radiative heating of the atmosphere (i.e., the subtraction of radiative effects from TOA to the surface in unit of  $\text{W} \cdot \text{m}^{-2}$ ). The model results were shown for the simulations for (a) IMPACT-Sphere-Mineral-V83 (E1) at the surface, (b) DustCOMM-Asphere-DB19-V83 (E2) at the surface, (c) E1 in atmospheric column, (d) E2 in atmospheric column, (e) E1 at TOA, and (f) E2 simulations at TOA. The numbers in parentheses represented the global

70 mean.

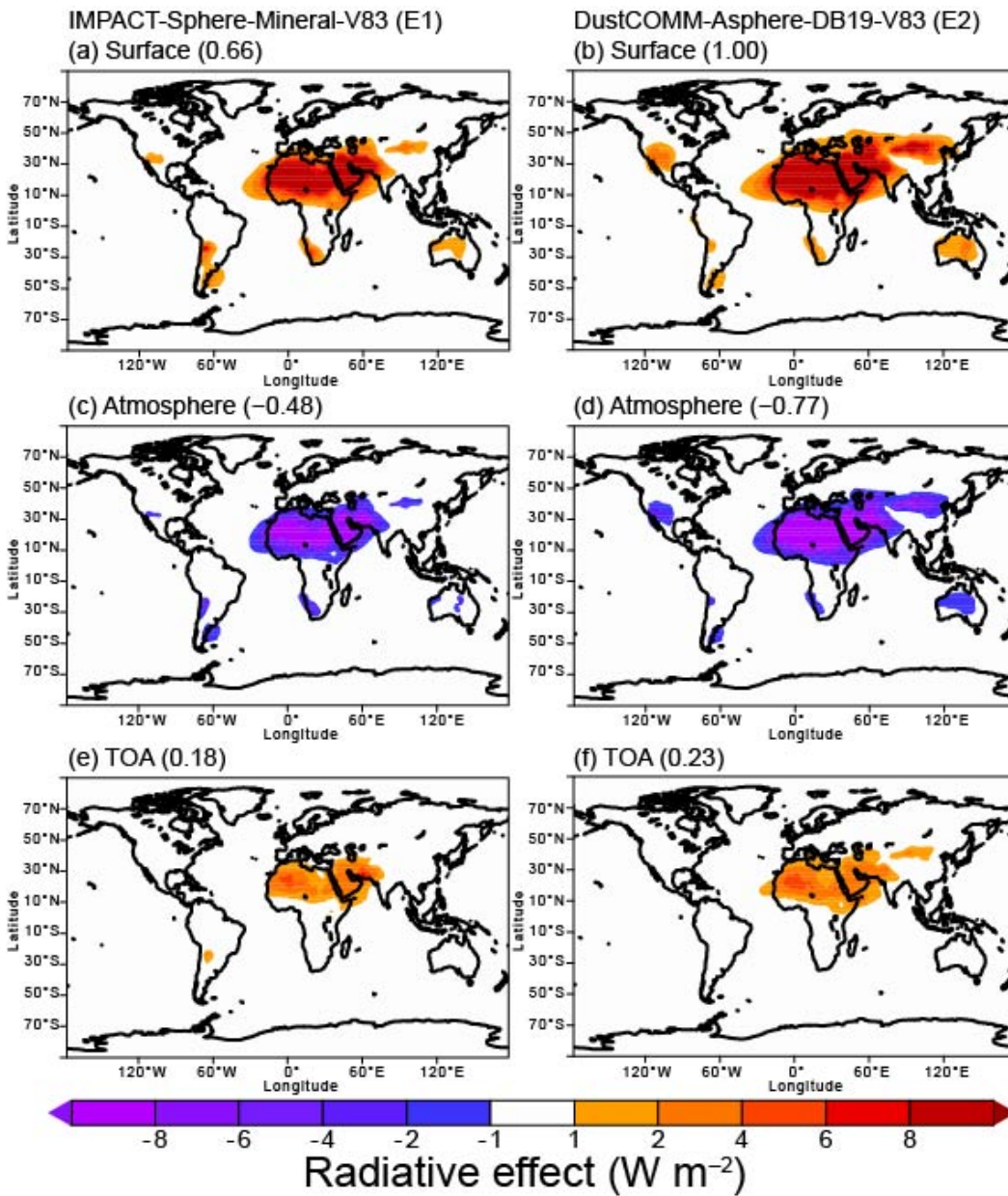


**Figure 7.** Dust LW radiative effect ( $\text{W}\cdot\text{m}^{-2}$ ) and radiative heating of the atmosphere (i.e., the subtraction of radiative effects from TOA to the surface in unit of  $\text{W}\cdot\text{m}^{-2}$ ). The model results were shown for the simulations for (a) IMPACT-Sphere-Mineral-V83 (E1) at the surface, (b) DustCOMM-Asphere-DB19-V83 (E2) at the surface, (c) E1 in atmospheric column, (d) E2 in atmospheric column, (e) E1 at TOA, and (f) E2 simulations at TOA. The numbers in parentheses represented the global mean.

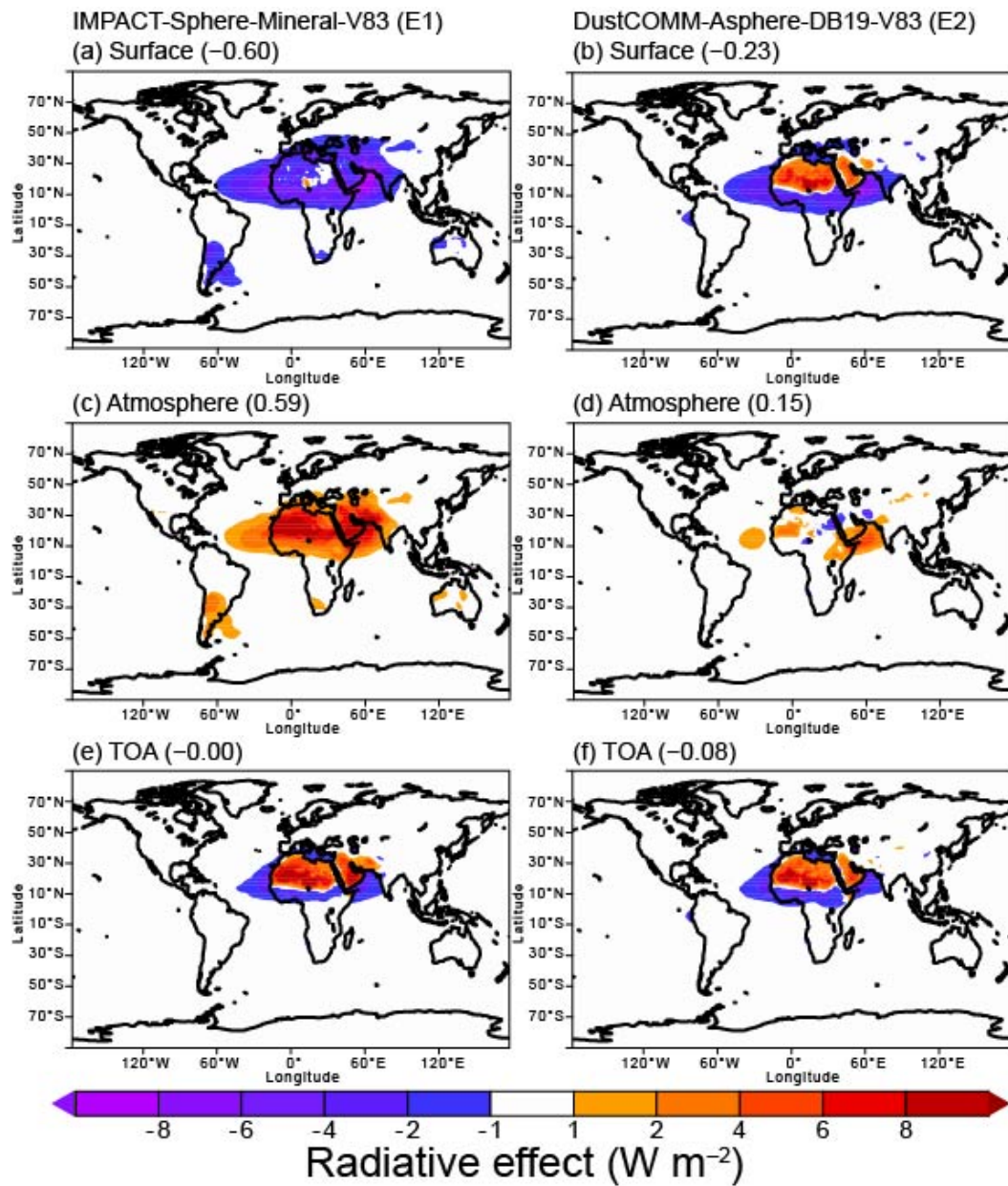
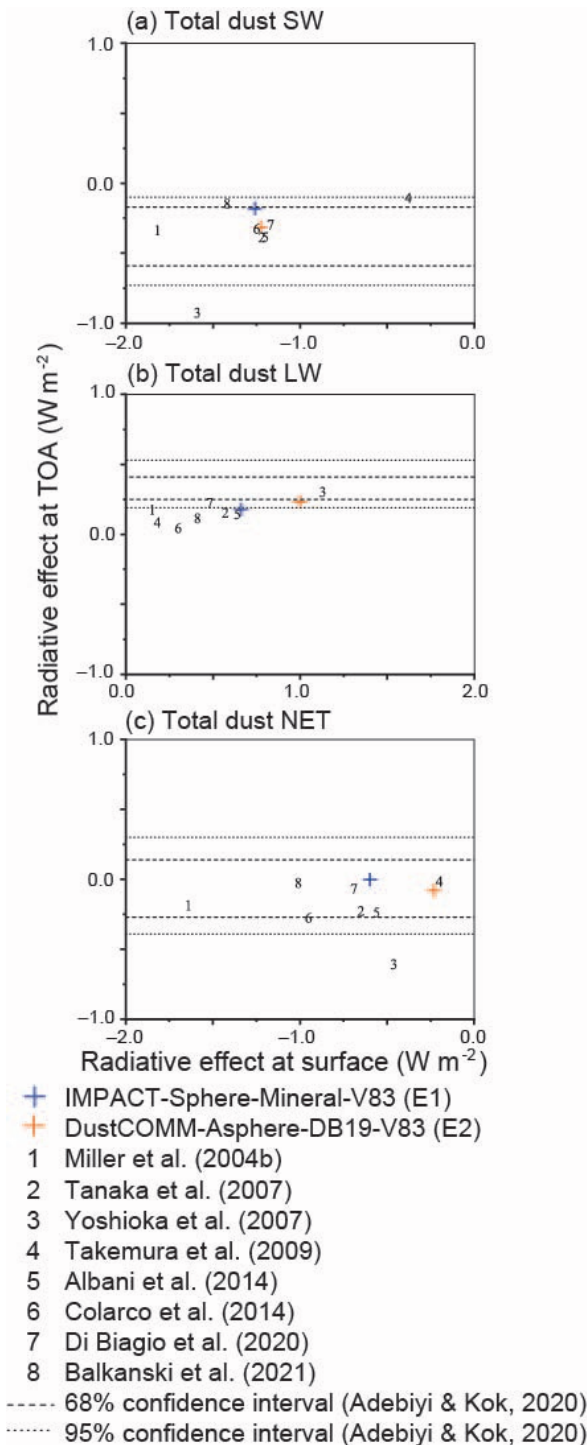


**Figure 8.** Dust net radiative effect ( $\text{W}\cdot\text{m}^{-2}$ ) and radiative heating of the atmosphere (i.e., the subtraction of radiative effects from TOA to the surface in unit of  $\text{W}\cdot\text{m}^{-2}$ ). The model results were shown for the simulations for (a) IMPACT-Sphere-Mineral-V83 (E1) at the surface, (b) DustCOMM-Asphere-DB19-V83 (E2) at the surface, (c) E1 in atmospheric column, (d) E2 in atmospheric column, (e) E1 at TOA, and (f) E2 simulations at TOA. The numbers in parentheses represented the global mean.



85 **Figure 9.** Variability of dust radiative effect ( $W \cdot m^{-2}$ ) in different model simulations at the surface and TOA for (a) total dust SW, (b) total dust LW, and (c) total dust NET. The annually averaged values were listed in Table 5.

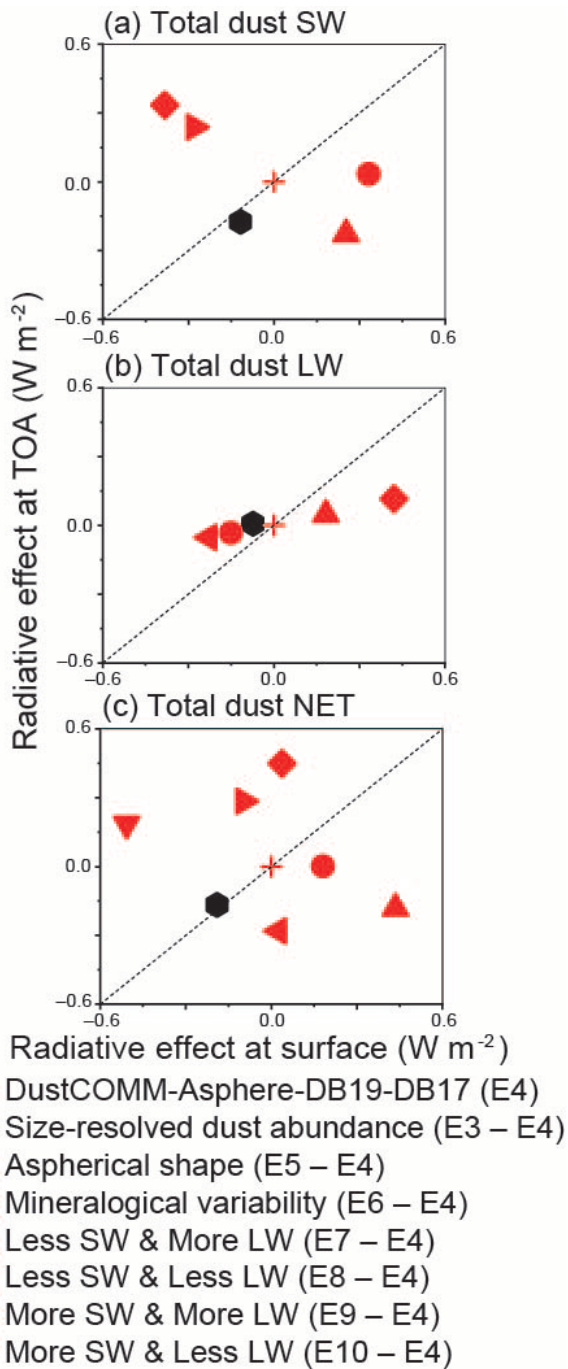


**Figure 10.** Radiative effect ( $W \cdot m^{-2}$ ) of mineral dust due to various aerosol absorptivity at the surface and TOA for (a) total dust SW, (b) total dust LW, and (c) total dust NET. The annually averaged values were listed in Table 5. The dashed line

90 represented a 1 : 1 correspondence and corresponded to no change in radiative heating within the atmosphere.